

Work-hardening exhaustion as the origin of low toughness in L-PBF alloys: A case study on the role of intrinsic vs. extrinsic defects in SS316L

KenHee Ryou^{1†}, Yaozhong Zhang^{1†}, James A. D. Ball², Dan Rubio-Ejchel¹, Dillon Jobes¹, Buhari Ibrahim¹, Charles Romain³, Henry Proudhon⁴, Jerard V. Gordon^{1*}

¹ Department of Mechanical Engineering, University of Michigan, Ann Arbor MI, 48109

² ESRF, The European Synchrotron, 71 Avenue des Martyrs, CS40220, 38043 Grenoble Cedex 9, France

³ ENSCM, Hétérochimie Moléculaire & Macromoléculaire 8, rue de l'Ecole Normale, Montpellier, France

⁴ Mines Paris, PSL University, MAT – Centre des matériaux, CNRS UMR 7633, BP 87, 91003, Evry, France

* Corresponding author: Dr. Jerard V. Gordon

Email addresses: jerardvg@umich.edu

† Equal Contribution

Abstract

Laser powder bed fusion (L-PBF) additive manufacturing offers a remarkable balance of strength and ductility across many structural alloys. However, L-PBF alloys often display much lower fracture toughness, in some cases up to 70% below conventionally wrought counterparts. The reasons for this “toughness paradox” have remained elusive, since conventional tools cannot directly visualize sub-surface microscale deformation processes that govern crack growth. Here we apply scanning 3D X-ray diffraction and phase contrast tomography to simultaneously capture microstructural evolution with 1 μm resolution near an advancing crack tip, utilizing 316L stainless steel as a model system. We demonstrate that the “toughness paradox” is not solely a consequence of extrinsic processing defects or residual stresses, but rather an intrinsic failure to relax crack-tip stresses via plasticity. While wrought material facilitates stable crack-tip blunting through localized dislocation accumulation, the L-PBF material undergoes premature work-hardening saturation that triggers extreme stress partitioning and high stress triaxiality. This results in a transition from ductile blunting to a sharp, unstable fracture mode. These findings identify work-hardening exhaustion as a systemic vulnerability inherent to L-PBF microstructures, where the exceptional initial dislocation density required for high yield strength acts as a saturation ceiling for damage tolerance. This work provides a physical basis for adapting damage models to L-PBF metals and challenges the assumption that high tensile ductility guarantees fracture resistance in rapidly solidified components.

Keywords: High-energy diffraction microscopy; damage tolerance; strain localization; austenitic stainless steel; crystallographic texture

1. Introduction

The emergence of laser powder bed fusion (L-PBF) additive manufacturing (AM) has fundamentally redefined the limits of structural alloy design [1,2]. By leveraging extreme cooling rates ($\sim 10^6$ K/s) and complex thermal cycles, L-PBF generates hierarchical microstructures characterized by dense sub-micron cellular networks, solute segregation, and high dislocation densities that

break the classical trade-off between strength and ductility [3]. For example, 316L stainless steel produced via L-PBF consistently exhibits tensile properties that surpass its conventionally wrought counterparts [4]. However, a critical bottleneck restricts the deployment of these materials in safety-critical applications: despite their high tensile ductility, recent studies have shown that the fracture toughness of L-PBF Fe, Ti, and Al alloys can drop by as much as 70% compared to wrought versions [1,2,5]. This disparity presents a fundamental mechanical paradox: *why do materials that excel in uniform tensile elongation fail so prematurely in the presence of a sharp crack?*

Fracture toughness is a critical measure of a material's capacity to dissipate energy and blunt a stress concentration through localized plastic work [6–8]. This property governs reliability and structural integrity under numerous applications from static loading to leak-before-break safety margin in pressure vessels and the life-limiting crack sizes that govern fatigue failure under cyclic loads [6,9]. In conventionally processed ductile metals, fracture is traditionally modeled through the nucleation, growth, and coalescence of micro voids—processes often described by models such as the Rice-Tracey or Gurson-Tvergaard-Needleman frameworks [10–12]. In these defect-centric theories, failure is driven by second-phase inclusions and manufacturing flaws. Consequently, the lower toughness of L-PBF alloys has often been cited as a consequence of manufacturing-related flaws, specifically the prevalence of processing defects including porosity and oxide inclusions.

A similar reduction in fracture resistance is well-documented in conventionally cold-rolled and severely plastically deformed (SPD) alloys [6,13,14]. In fully dense SPD materials, the exhaustion of work-hardening capacity—driven by dislocation densities nearing saturation can instead promote toughness loss [8,15,16]. Recent landmark studies in high-purity face-centered cubic (FCC) metals have further demonstrated that ductile fracture can be dominated by shear-driven localization rather than traditional void growth, even when particles are present [11,17,18]. In the context of AM alloys, it remains unclear whether the toughness deficit is an extrinsic result of process-induced porosity or an intrinsic byproduct of the pre-existing dislocation networks, residual stress distributions, and crystallographic textures that may suppress crack-tip blunting and energy dissipation.

However, the assumption that porosity is the sole (or most important) driver of the AM toughness deficit is being increasingly contested [5,19,20]. A similar inverse relationship between strength and fracture resistance is well-established in ultrafine-grained and SPD alloys [21,22]. In these fully dense materials, the exhaustion of work-hardening capacity—resulting from dislocation saturation and restricted mean free path—induces early plastic instability, thereby severely limiting the plastic zone size and energy dissipation at the crack tip [21,22]. Recent micromechanical studies in high-purity FCC metals have further demonstrated that ductile fracture can be dominated by shear-driven localization rather than traditional void growth, particularly when strain hardening rates are low [11,17,18]. In the context of AM alloys, it remains unclear whether the toughness deficit is an extrinsic result of process-induced porosity or an intrinsic byproduct of the pre-existing dislocation networks and crystallographic textures that suppress the crack-tip blunting mechanisms essential for high toughness.

The inability to resolve this debate stems from a fundamental observation gap. The mechanical state surrounding an active, moving crack involves a singular stress state and extreme local strain gradients [10]. Capturing these states at the crystal scale is a formidable challenge where conventional tools such as surface-based digital image correlation or post-mortem electron backscatter diffraction are fundamentally limited. Surface-level measurements fail to capture the high-triaxiality stress states that exist in the bulk where fracture initiates, and the extreme local strains often lead to pattern decorrelation or indexing losses, rendering the most critical regions of the crack tip

unobservable to researchers [23,24]. Furthermore, while three-dimensional (3D) techniques such as absorption or phase-contrast tomography (PCT) can resolve the morphology of void nucleation and growth, they cannot explicitly measure the underlying crystallographic orientation, internal stresses, or dislocation densities that govern local crack-driving forces [25]. Consequently, researchers have been forced to infer bulk behavior from surface observations, leaving the competition between extrinsic manufacturing defects and intrinsic microstructural effects largely unquantified.

In this work, we bridge this gap by employing high-energy scanning 3D X-ray diffraction (s3DXRD) in tandem with companion PCT at the European Synchrotron Radiation Facility (ESRF) [26]. This dual-modal approach provides a non-destructive, volumetric visualization of full-field orientations and the complete 3D strain tensor within hundreds of individual grains surrounding an advancing crack tip. This volumetric resolution enables the quantification of internal stress fields and Geometrically Necessary Dislocation (GND) densities within the interior of the specimen, providing a direct view of the crack-tip mechanics that remain inaccessible to surface-level characterization. This allows for a direct, quantitative assessment of the competition between manufacturing-induced defects and intrinsic microstructural features in bulk samples under conditions most representative of real-world failure. Such high-fidelity mapping provides the experimental framework required to decouple the roles of process porosity and dislocation-mediated plasticity in the fracture of L-PBF alloys.

Using 316L stainless steel as a model system, we leverage these unique experimental tools to rigorously decouple the primary drivers of the AM toughness deficit [1,5]. We evaluate two competing mechanisms: (i) an extrinsic pathway where process-induced porosity facilitates rapid crack propagation via discrete ‘void-capture’, and (ii) an intrinsic pathway where high initial dislocation densities lead to premature work-hardening saturation. This saturation reduces plastic deformation, leading to localized high-stress bands which prevent energy dissipation to blunt the crack tip. Integrating these observations across a series of synchronized crack mouth opening displacements (CMOD) provide a holistic view of how the hierarchical AM microstructures govern the mechanistic evolution of the crack-tip field during failure. Resolving the sub-surface micromechanical response within the specimen interior—where triaxial constraint is most severe—uncovers the governing physics of the material's bulk response during an active fracture event. Overall, these data provide a new insight into the “toughness paradox” of L-PBF alloys, and how AM alloys must shift the focus from simple defect mitigation toward the fundamental microstructural engineering that enhances crack-tip plasticity for improved damage-tolerance.

2. Materials and Methods

2.1 Sample fabrication

Two samples were investigated in this study: (i) as-built L-PBF SS316L and (ii) a conventionally wrought and heat treated SS316L. Pre-alloyed gas atomized EOS SS316L powder (20 – 65 μm) was used to create as-built L-PBF AM test blocks on an EOS M290 machine using a Yb-fiber laser. Test blocks (35 mm \times 13.4 mm \times 5.5 mm) were printed in pure Ar atmosphere using a preheat temperature of 80°C. High-density samples were achieved using manufacturer recommended parameters including a laser power of 195 W, scanning velocity of 1083 mm/s, hatch spacing of 90 μm , layer thickness of 20 μm , and 67° interlayer rotation. For the wrought sample, hot-rolled SS316L plate was machined into blocks and subjected to a solution annealing treatment of 1050°C for 30 mins, followed by a rapid quench to achieve a fully austenitic, equiaxed

microstructure. Sub-sized “Nanox” geometry tensile specimens [27] (0.5 mm × 0.5 mm × 14 mm) were extracted from the center of both blocks via wire electro-discharge machining (EDM). For the L-PBF sample, the tensile axis was aligned parallel to the AM build direction. In comparison, the wrought sample tensile axis was aligned with the original rolling direction. A sharp mode-I notch was milled into each specimen to create an approximate $a/W = 0.4$ (where a is an initial crack length, approximately 0.2 mm and W is width of specimen, 0.5 mm) using a Thermo Fisher Helios G5 Hydra Plasma focused-ion beam at the University of Michigan to ensure a well-defined initiation point for crack advance.

The specimen dimensions were selected to optimize transmission for the synchrotron X-ray beam. Given the high ductility of 316L stainless steel, these dimensions result in a stress state dominated by plane stress conditions, as the sample thickness is significantly below the requirement for valid plane-strain fracture toughness measurements [7,28]. Consequently, the fracture toughness values reported herein focus on elastoplastic crack tip opening displacement (CTOD) or comparative K_{Ic} (conditional) estimates, serving to contrast the relative resistance of the L-PBF and wrought microstructures rather than providing absolute standard design values.

2.2 *In-situ loading and Data Acquisition*

In-situ fracture experiments were performed under load control at the ESRF on beamline ID11 [29]. Loading was performed using the “Nanox” miniature stress rig [27], which utilizes a piezoelectric actuator for precise control up to 500 N. This device is specifically optimized for tensile and fatigue testing within a synchrotron environment. The data acquisition sequences for both specimens are detailed in Table 1.

To account for the $\sim 2\times$ disparity in yield stress (YS) between the L-PBF and wrought SS316L materials (**Fig. 5a**), X-ray measurements of each sample were synchronized via CMOD values. This ensured that observations of crack-tip phenomena remained analogous across both materials. CMOD values were derived directly from PCT data of the notch. The experimental setup at ID11 utilized a 43.57 keV monochromatic X-ray beam and an Eiger2 4M CdTe detector positioned at 150 mm. PCT was performed at a 0.93 μm pixel resolution to enable volumetric imaging of internal voids, notch blunting, and crack propagation. To mitigate stress relaxation and creep, X-ray measurements at each load step (L0–L8) were acquired following a 20% partial unloading in accordance with ASTM E1820.

S3DXRD was employed to map orientation and elastic strain fields within a volume of 500 $\mu\text{m} \times 350 \mu\text{m} \times 50 \mu\text{m}$ centered at the notch tip. Using a beam size of 1.02 $\mu\text{m} \times 1.3 \mu\text{m}$, between 3–6 layers were scanned per load step at 6.5 μm intervals. For each layer, the sample was rotated 180° in 0.05° increments with a 2 ms exposure, generating ~ 2.6 million diffraction patterns (1.2 TB) over approximately 2.5 hours. PCT was conducted before each s3DXRD scan to ensure centering after load-induced displacement. Finally, surface roughness from sample preparation was used to register the tomography datasets with s3DXRD slices across all load steps.

Table 1. *In-situ* experimental organization for combined s3DXRD and PCT.

Stage	L0	L1	L2	L3	L4	L5	L6	L7	L8	
L-PBF	CMOD (μm)	29.1	30.8	32.6	38.4	63.1	72.1	86.0	99.2	127.2
	Load (N)	7	20	40	60	74	73	72	71	64
	PCT data	○	○	○	○	○	○	○	○	○
	s3DXRD (# of layers)	○ (3)	-	-	-	○ (5)	○ (5)	-	○ (6)	-
	CMOD (μm)	29.3	30.9	39.8	47.6	52.8	65.5	91.6	123.2	140.8
Wrought	Load (N)	3	20	40	45	47	52	58	63	65
	PCT data	○	○	○	○	○	○	○	○	○
	s3DXRD (# of layers)	○ (3)	-	-	○ (5)	-	○ (5)	○ (3)	-	-

2.3 Data Reconstruction

PCT data were reconstructed using the Nabu software package, developed at the ESRF [30]. A large field of view was utilized to capture the entire notch region and surrounding material, facilitating subsequent data registration with s3DXRD volumes at each load step. Reconstruction of s3DXRD data [31] was performed using ImageD11 [32], following the workflow established by Zhang et al. [26]. Approximately 200 million diffraction peaks were segmented and labeled per layer from the raw detector images. Peaks smaller than 15 pixels were discarded as noise. To isolate the austenitic phase, peaks were filtered based on the SS316L lattice parameter, retaining only those within 0.005 \AA^{-1} in d^* of predicted diffraction ring positions. This reduced the dataset to ~ 67 million peaks per layer. To optimize indexing speed, only the (111), (200), (220), (222), (400), and (440) rings were utilized. A point-by-point indexing strategy was employed on an approximately 559×559 square reconstruction grid with a $1 \mu\text{m}$ spacing to match the beam size and translation step [33]. For each voxel, input peaks were masked via a path on the sinogram in (y, ω) space to isolate potential origins. Candidate orientations were generated and scored; orientations were accepted if they indexed at least 70% of the predicted peaks. To account for voxels containing grain boundaries, multiple candidate solutions were stored if they indexed at least 60% of the maximum number of peaks found for any grain at that voxel.

Following initial indexing, a less-stringent peak filtration was applied to include higher-angle rings, resulting in a dataset of ~ 152 million peaks per layer. After correcting each peak for its origin of diffraction, the grain orientations and strain tensor elements were refined using the approach outlined by Henningsson et. al [34]. Reconstructions for body-centered cubic (BCC) martensite (α') phases were conducted using an identical peak indexing and refinement process in Ball et. al [35].

3. Results

3.1 Initial microstructure and defect density

The initial PCT and s3DXRD data acquired prior to loading reveal the initial microstructure and defect densities of both samples within the notch region (**Fig. 1**). The PCT data enables direct identification of the initial notched specimen geometry. As indicated by the red and blue dashed lines extracted from these data, the evolution of the crack tip can be tracked across loading stages, showing a progressive reduction in cross-sectional area and a gradual growth of the crack tip relative to its initial position. The s3DXRD analyses were performed over multiple layers within

the volume surrounding the notched region, allowing characterization of the grain structure prior to and after deformation. The LPBF specimen exhibits typical irregular grain structure, with a strong crystallographic texture (**Fig. 1a**). In contrast, the wrought specimen shows an equiaxed grain morphology and a more uniformly distributed crystallographic orientation (**Fig. 1b**).

Fig. 1c and **d** show the size distribution of grains and pores of both samples. LPBF sample exhibits a similar grain size (median value of 15.1 μm grain diameter) compared to the wrought sample (median value of 17.5 μm). While the wrought sample contains grain boundaries consisting mainly of high-angle grain boundaries (44.9%) and twin boundaries (53.4%), with only 1.7% low-angle grain boundaries, the L-PBF sample contains 52.7% low-angle grain boundaries (**Fig. 1c**). Both samples are well above 99.98% bulk density (the L-PBF sample shows a volume fraction of pores slightly higher but statistically comparable volume fraction, see **Fig. 1d**). Such low defect densities have shown negligible impact on mechanical properties in AM alloys [36,37]. Furthermore, differences in size distribution and maximum of pores in both samples are statistically insignificant (**Fig. 1d**). These results highlight that initial defect densities and grain sizes are largely similar between the L-PBF and wrought sample, enabling a robust assessment of the competition between extrinsic and intrinsic properties on toughness between these two materials.

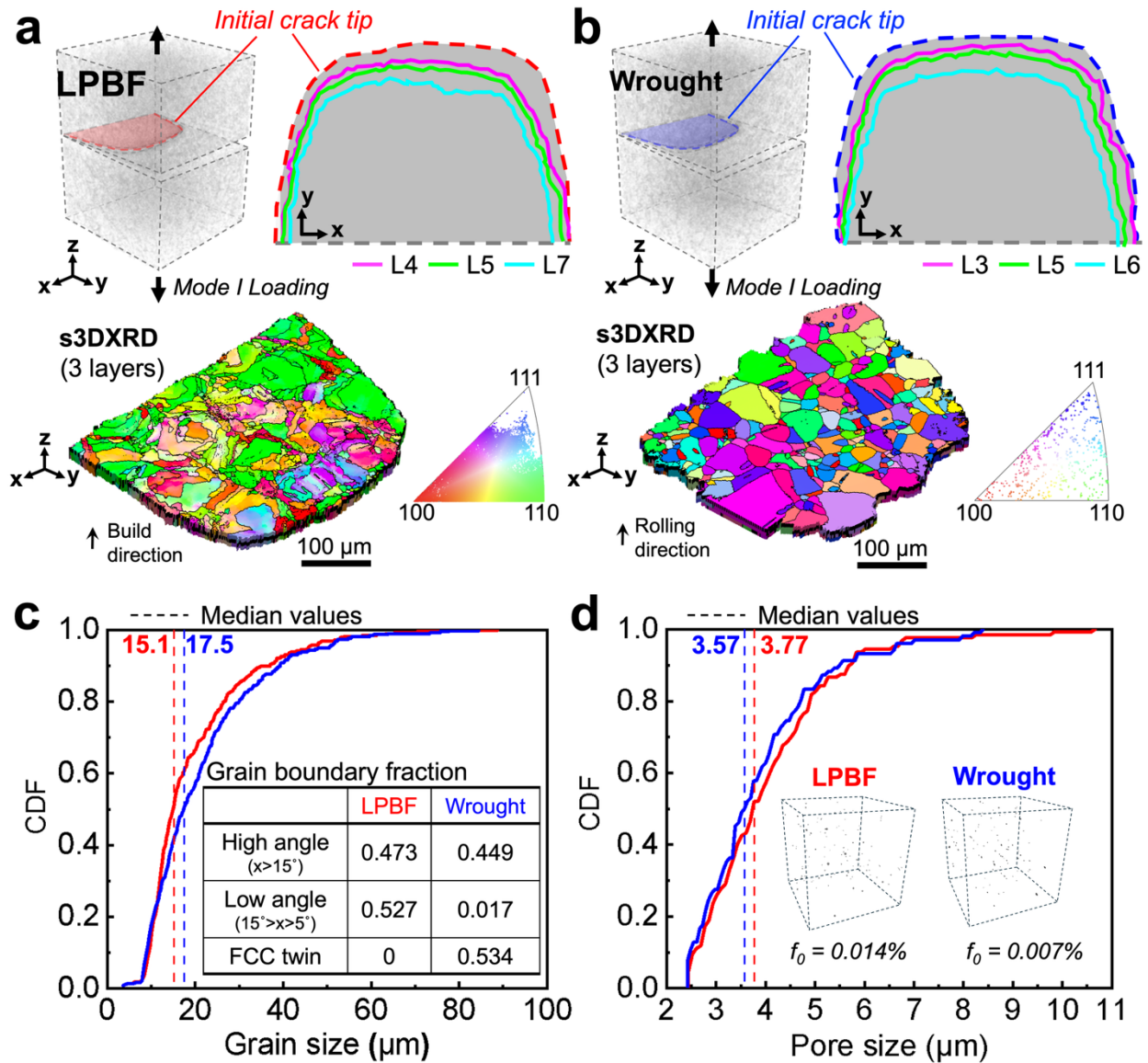


Fig. 1. (a) Inverse Pole Figure (IPF-Z) map of the L-PBF SS316L specimen showing the characteristic $\langle 110 \rangle$ texture along the build direction. (b) IPF-Z map of the Wrought SS316L specimen displaying an equiaxed grain morphology. (c) CDF comparing grain size (area) and grain boundary character between the two material conditions. (d) Comparative pore size distributions indicating statistically similar defect populations in both L-PBF and Wrought samples.

3.2 Crack tip advance and driving force

The macroscopic mechanical behavior of the L-PBF and wrought specimens was evaluated by correlating the load response with crack extension, CMOD, and CTOD. The PCT data during loading enabled tracking the overall notch shape and crack tip advance, where selected stages show gradual evolution (**Fig. 2a**). The definitions of CMOD and CTOD are illustrated on the cross-section from the stage L8 PCT data. CMOD was defined as the distance measured outside the notch (blue colored arrow in **Fig. 2a**) [38]. CTOD was defined by first identifying the midpoint of the crack along the tensile loading direction and fitting an approximate centerline (black dotted

line in **Fig. 2a**). From the point at which this line reaches at the crack tip, two lines inclined at $\pm 45^\circ$ with respect to the centerline (orthogonal to each other with a total included angle of 90°) are drawn. CTOD was determined using two methods: (i) direct measurement from the reconstructed PCT data based on the work of Toda et. al [38] (shown by green colored line in **Fig. 2a**), and (ii) calculation from CMOD values following ASTM standard E1820. This enables direct comparison between the *in-situ* results in this study and other studies leveraging bulk (CMOD derived) testing. Based on ASTM E1820, the total CTOD is partitioned into elastic (δ_e) and plastic (δ_p) components:

$$CTOD (\delta) = \delta_e + \delta_p = \frac{K^2(1-\nu^2)}{E\sigma_Y} + \alpha_{geom}(CMOD - C_{elastic}P) \quad (1)$$

where ν is Poisson's ratio (0.3), E is elastic modulus (193 GPa), σ_Y is YS (525 MPa for LPBF and 303 MPa for wrought), α_{geom} is the geometric scaling factor ($CTOD_p/CMOD_p$, 0.31 for LPBF and 0.65 for wrought) determined experimentally, $C_{elastic}$ is the elastic compliance ($\Delta CMOD/\Delta P$, 8.9×10^{-5} for LPBF and 1.3×10^{-4} for wrought), and P is load. Mode I stress intensity factor K is calculated as below:

$$K = Y(a/W)\sigma_{net}\sqrt{\pi a} \quad (2)$$

where $Y(a/W)$ is a standard approximate shape function from Tada-Paris-Irwin type solution [39], σ_{net} is net-section stress $P/t(W-a)$, where t is thickness (0.5 mm) of specimen.

Fig. 2b illustrates the load response as a function of CMOD for both specimens. To ensure proper seating within the tensile grips, a marginal pre-load of $\sim 3-7$ N was applied at the initial stage (L0) resulting in a nominal axial tensile stress of $\sim 24 - 48$ MPa for both materials; these values are well below 20% of the YS and ensure an elastic baseline (**Fig. 5a**). Given the nearly identical cross-sectional geometries of both samples, the L-PBF specimen displayed a significantly higher load-bearing capacity throughout the initial loading stages compared to the wrought counterpart. After stage L4, the L-PBF sample undergoes softening, during which the applied load decreases. It is also confirmed that the crack growth with increasing CMOD in the L-PBF sample is greater than that in the wrought sample even before softening occurs, and the crack length increases further rapidly once softening begins (**Fig. 2c**).

The comparison between measured and calculated CTOD (**Fig. 2d**) reveals that the wrought sample maintains excellent agreement with the calculated values throughout the test. In contrast, the L-PBF sample shows a significant CTOD drop after stage L6. This discrepancy is reflected in the estimated conditional fracture toughness (K_q), calculated via the J-integral relation:

$$K_q = \sqrt{J \cdot E} = \sqrt{M\sigma_{flow}\delta \cdot E} \quad (3)$$

where J is the J-integral, M is constraint factor (1 for LPBF and 1.5 for wrought), and σ_{flow} is the flow stress (average of yield and ultimate strengths, 578 MPa for LPBF and 427 MPa for wrought). K_q was here analyzed to provide comparable results to bulk toughness results of other studies on SS316L such as Suryawanshi et. al [40] and since sub-size ‘‘Nanox’’ sample geometries do not meet specific plane-strain requirements for K -dominated testing.

As shown in **Fig. 2e**, the wrought sample exhibited a steady increase in toughness with crack extension, indicating a high resistance to propagation. This is shown by the significant increase in K_q of ~ 25 MPa \cdot m $^{1/2}$ at L3 to a maximum value of 100 MPa \cdot m $^{1/2}$ at L8 over a relatively small change in crack length ($\Delta a = 15$ μ m). Interestingly, the values for maximum K_q , while a conditional toughness value, match the range of expected K_{IC} values for wrought SS316L in the literature

($\sim 112 - 278 \text{ MPa}\cdot\text{m}^{1/2}$). In contrast, the L-PBF sample, although also showing an initial increase in toughness, fails to increase further after stage L6. The maximum value reached in the L-PBF sample is approximately $K_q = 65 \text{ MPa}\cdot\text{m}^{1/2}$, similar to the results of bulk compact tension samples used in Suryawanshi et. al [40] of $K_q = 72 \text{ MPa}\cdot\text{m}^{1/2}$ for this orientation (Note: a $K_q = 62.9 \text{ MPa}\cdot\text{m}^{1/2}$ was determined in [40] for orientations manufactured perpendicular to build direction, which suggests that toughness reductions in L-PBF are not solely a consequence of anisotropy). Overall, considering the level of crack extension, the L-PBF sample demonstrates significantly inferior fracture toughness compared to the wrought specimen. Additionally, these results highlight that while sub-sized specimens were used, the *in-situ* data used in this study can probe both bulk material behaviors and localized 3D imaging of the crack tip.

To better understand the evolution of the crack front and tip morphology, **Fig. 3** and **4** present PCT data to highlight fracture mechanisms in both samples. Different regions of the 3D PCT data were used to quantify local crack growth under two conditions in both wrought and L-PBF samples, namely: (i) steady state crack growth and (ii) crack growth in the presence of process-induced spherical pores. In the wrought sample, steady state crack growth exhibits a stable, self-similar propagation throughout the loading sequence. Superimposed images of the x-y plane (perpendicular to the loading direction) show that the edge lines for stages L4 through L8 retreat uniformly (**Fig. 3a**). This stable growth is further evidenced in the y-z plane views (perpendicular to the notch front) of the interior region, where the deformation is dominated by continuous crack tip blunting rather than the initiation of new features (**Fig. 3b-e**). Even when the propagating crack encounters pre-existing porosity (diameter $\sim 6\mu\text{m}$), this blunted morphology is maintained (**Fig. 3d**); as the crack front reaches the pore, it integrates the defect without forming a sharp stress concentrator, preserving a rounded, pore-like tip profile (**Fig. 3e**). Furthermore, 3D observations reveal that the pore enlarges during deformation and becomes noticeably elongated along the loading axis (**Fig. 3f**).

In contrast, the LPBF sample demonstrates a distinct transition in fracture mode that leads to unstable crack advance (**Fig. 4**). The x-y plane reconstructions reveal significant spatial irregularities in the crack front retreat, particularly in the region highlighted by the lower arrow in **Fig. 4a**, where the edge lines show a non-uniform progression between stages L5 and L6. Imaging of the y-z plane in this region confirms that at stage L6, the previously blunted crack tip undergoes a localized transition to a sharp fracture mode, as indicated by the rapid initiation of a sharp extension from the notch front (**Fig. 4b-c**). This sharp profile continues to develop through the final loading stages (L7 and L8), representing a marked departure from the ductile behavior seen in the wrought sample. A similar fracture mode transition occurs near internal pores in **Fig. 4d-e**; this defect is likely a spherical keyhole or entrapped gas pore with size $\sim 6 \mu\text{m}$ in diameter [36]. At stage L6, a sharp crack front initiates and propagates aggressively toward and through the pore, bypassing the stabilizing effect of plastic blunting and leading to a sharp, secondary protrusion (**Fig. 4d-e**). In addition, it is noticeable from the 3D reconstruction that the pore enlarges during deformation but does not elongate in the L-PBF sample (**Fig. 4f**). Overall, our results highlight significant differences in ductile crack growth between wrought and L-PBF samples for both steady state crack advance and local growth modes in the presence of (similar sized) pore defects. These differences will be more closely examined in the following sections to understand the role of microstructure and internal stress distributions driving these behaviors.

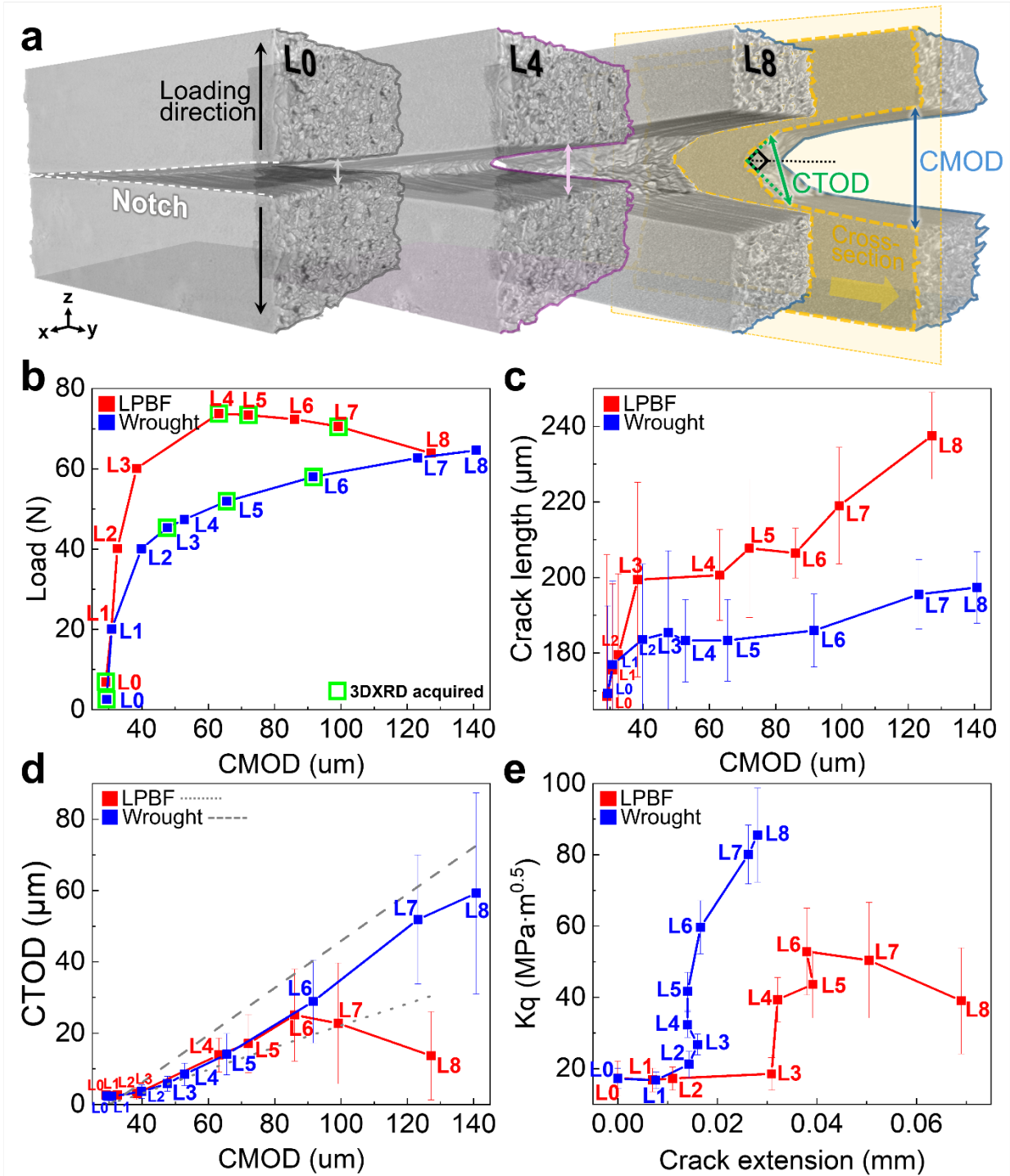


Fig. 2. Macroscopic fracture response. (a) PCT images of notch shape and crack tip advance captured. (b) Load versus CMOD curves. (c) Crack extension (Δa) plotted against CMOD. (d) Measured versus calculated CTOD. (e) Conditional fracture toughness (K_q) resistance curves, demonstrating the significant toughness deficit in the L-PBF alloy compared to the Wrought counterpart.

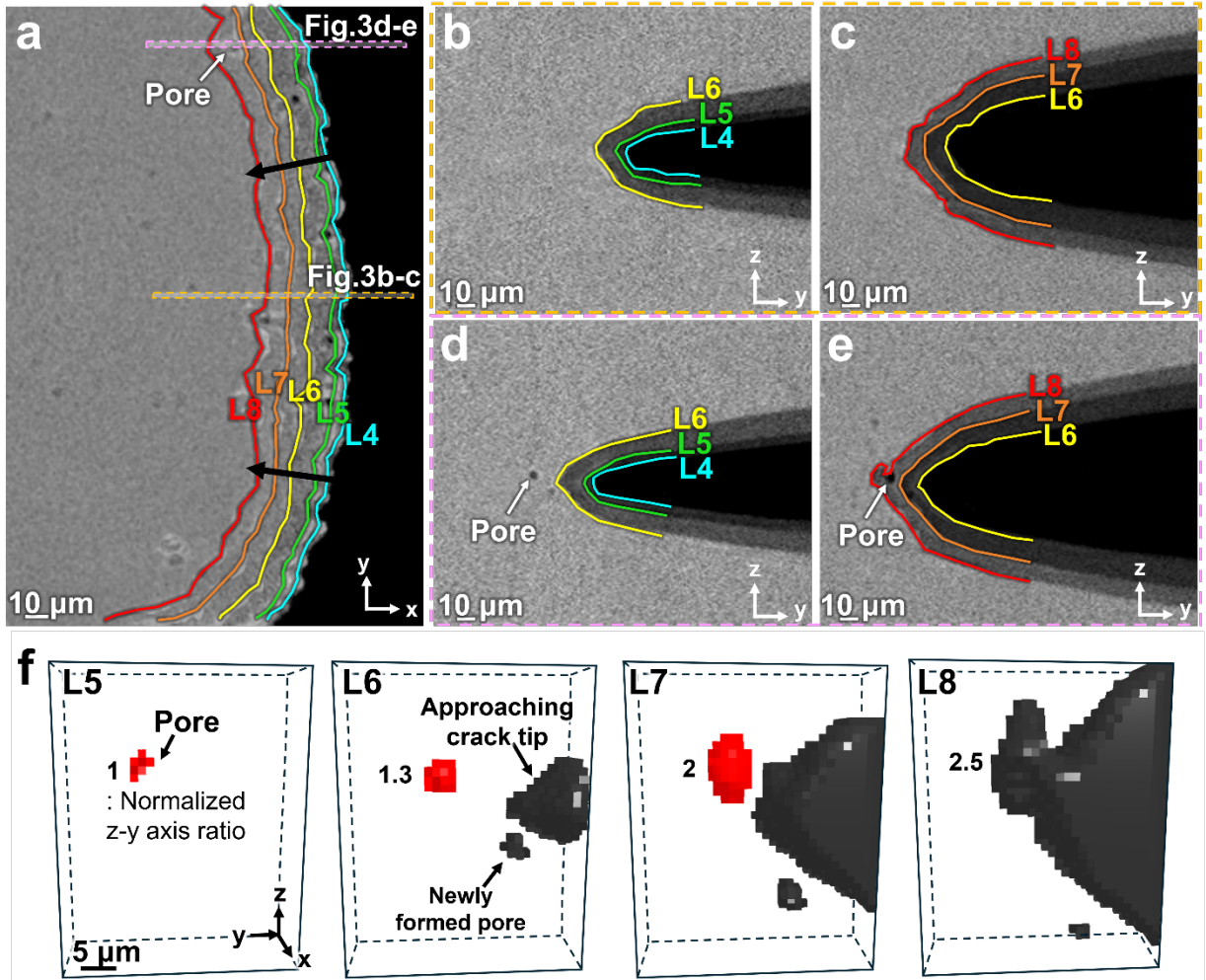


Fig. 3. Stable crack growth in Wrought SS316L observed via in-situ PCT. (a) X-Y plane view of crack front retreat. (b-e) Y-Z cross-sections showing continuous crack tip blunting and interaction with internal porosity. (f) 3D reconstruction of pore and crack tip evolution corresponding to Fig. 3d-e.

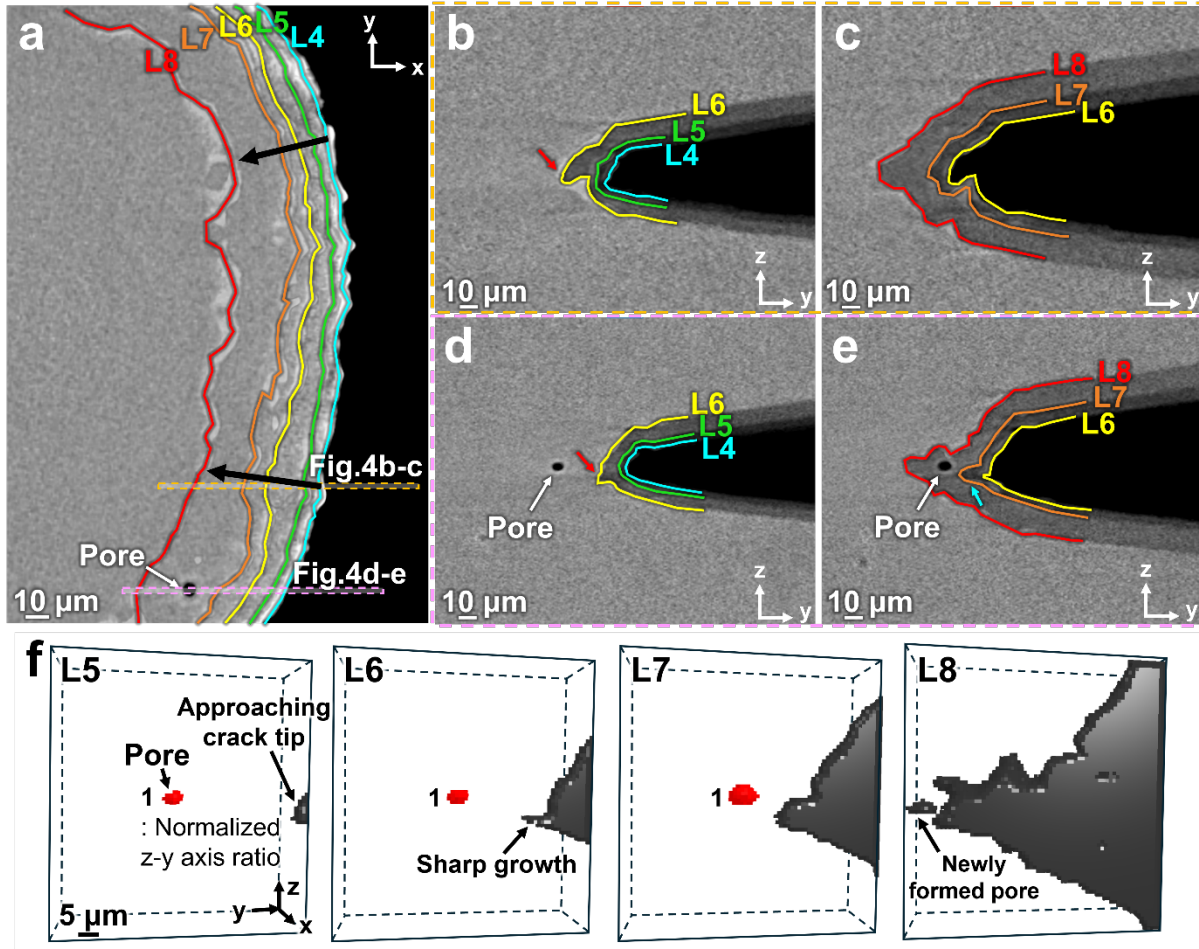


Fig. 4. Unstable fracture in L-PBF SS316L observed via in-situ PCT. (a) Irregular crack front progression. (b-c) Transition from blunting to sharp fracture. (d-e) Crack tip interaction with a process-induced pore leading to sharp instability. (f) 3D reconstruction of pore and crack tip evolution corresponding to Fig. 4d-e.

3.3 Evolution of local crack tip micromechanical fields

3.3.1 Internal residual stresses

To identify the microscale driving forces behind differences in crack growth behaviors for wrought and L-PBF samples, the spatial distribution and evolution of 3D internal stress states were quantified using voxelized s3DXRD data. To account for stress state multiaxiality in the presence of a crack tip, the spatial distribution of intragranular (type III) von Mises stresses in each layer were quantified [41]. Such crystal-scale quantification allows for facilitates a detailed understanding of load partitioning and the multiaxiality of deformation (e.g., encompassing both axial and bending components), while providing the necessary basis for calculating stress triaxiality in subsequent analyses.

Intragranular von Mises stresses were determined by first converting the strain tensor of each voxel (ϵ^{grain}) in the crystal frame to the Cauchy stress tensor for each voxel (σ^{grain}) via the elastic stiffness tensor (C) for SS316L [3] using Hooke's law:

$$\boldsymbol{\sigma}^{\text{grain}} = \boldsymbol{C} : \boldsymbol{\varepsilon}^{\text{grain}} \quad (4)$$

The stress deviator tensor ($\boldsymbol{s}^{\text{grain}}$) for each voxel was determined by removing the hydrostatic component:

$$\boldsymbol{s}^{\text{grain}} = \boldsymbol{\sigma}^{\text{grain}} - \frac{\text{tr}(\boldsymbol{\sigma}^{\text{grain}})}{3} \mathbf{I} \quad (5)$$

where $\text{tr}(\boldsymbol{\sigma}^{\text{grain}})$ is the trace of the stress tensor and \mathbf{I} is the identity matrix. Finally, the von Mises stress (σ_{VM}) was calculated for each voxel using the second invariant (J_2) of the stress deviator:

$$J_2 = \frac{1}{2} \text{tr}(\boldsymbol{s}^{\text{grain}} \cdot \boldsymbol{s}^{\text{grain}}) \quad (6)$$

$$\sigma_{VM} = \sqrt{3J_2} \quad (7)$$

For reference, a representative engineering stress-strain curve for identical, un-notched sub-sized samples is presented in **Fig. 5a**. These uniaxial tensile properties for both L-PBF (0.2% offset YS of 525 MPa, tensile strength of 630 MPa, and elongation to failure of 60%) and wrought (0.2% offset YS of 303 MPa, tensile strength of 550 MPa, and elongation to failure of 75%) show excellent strength and ductility, with values in the expected ranges of sub-sized SS316L samples with machine surfaces [42–44].

The evolution of internal stresses (given by average σ_{VM}) as a function of the applied CMOD is shown in **Fig. 5b**. Here, a stark contrast exists in the bulk response of L-PBF and wrought specimens. In the initial state (L0), both samples begin with relatively low internal stresses between ~100 and 200 MPa. Specifically, the LPBF sample starts at an elevated baseline of 193 MPa, compared to 149.8 MPa for the wrought sample; these differences are attributed to the effect of the pre-load to seat the sample prior to loading described in Section 2.1 in addition to inherent thermal residual stresses produced during the AM processing. As loading progressed, the average σ_{VM} for the LPBF sample increased drastically, reaching ~733 MPa at stage L4 and peaking at ~819 MPa by stage L7. Remarkably, this average internal stress in the LPBF material eventually exceeded its macroscopic ultimate tensile strength (UTS), with maximum values greater than 1 GPa at L7. In contrast, the wrought sample exhibited significantly reduced stress increases, reaching just 355.5 MPa by stage L6 – a value that only slightly exceeded the macroscopic YS. This lower increase in stress for the wrought material at a similar CMOD suggests more extensive plasticity and subsequent stress relaxation compared to the L-PBF sample.

The spatial distribution of intragranular σ_{VM} at the crack tip further illuminate differences between L-PBF and wrought behaviors. For the L-PBF specimen shown in **Fig. 6a**, significant stress localization at the crack tip with stresses exceeding 1 GPa are visible as early as L4. Interestingly, in addition to the expected elevated stresses at the crack tip, widespread internal σ_{VM} "hotspots" are also visible, indicating severe stress partitioning [34,45]. Corresponding 1-D line profiles (**Fig. 6c**) confirm both stress localizations near the crack tip, in addition to interior partitioning behaviors shown by jagged stress distributions between 600 and 900 MPa. The wrought sample also shows elevated stresses near the crack tip, the overall σ_{VM} magnitude is much lower than L-PBF and more uniform, with magnitudes generally plateauing between 300 and 450 MPa (**Fig. 6b**). While significant stress partitioning also is evident in wrought sample, this occurs more gradually and more homogenous than the L-PBF sample.

Overall, internal stress states, while starting out similar at L0, evolve very differently between wrought and L-PBF with additional loading and crack advance. Importantly, these internal stress partitioning may offer new insights into local stress distribution mechanisms in the presence of a crack tip and are potentially linked to the evolution of dislocation substructures during loading. The link between internal stress states and plasticity which will be further quantified via GND distributions in Section 3.4, while the roles of stress partitioning behaviors and pre-existing dislocation sub-structures on crack-tip driving forces will be further discussed in Section 4.2.

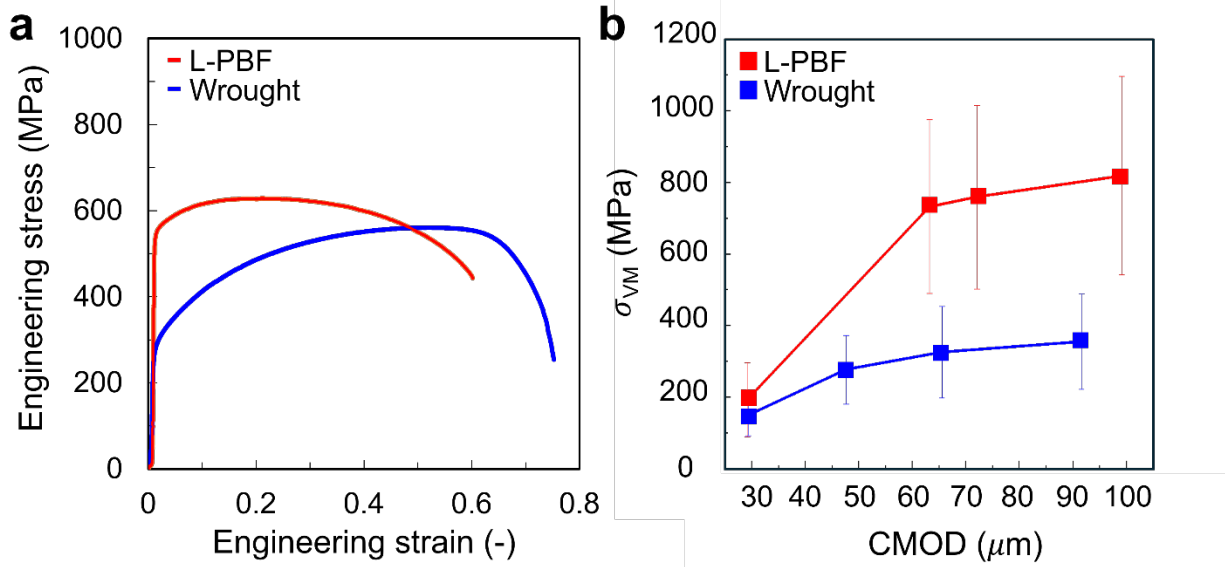


Fig. 5. Global and local stress evolution. (a) Uniaxial engineering stress-strain curves. (b) Evolution of volume-averaged von Mises stress within the notch region vs. CMOD.

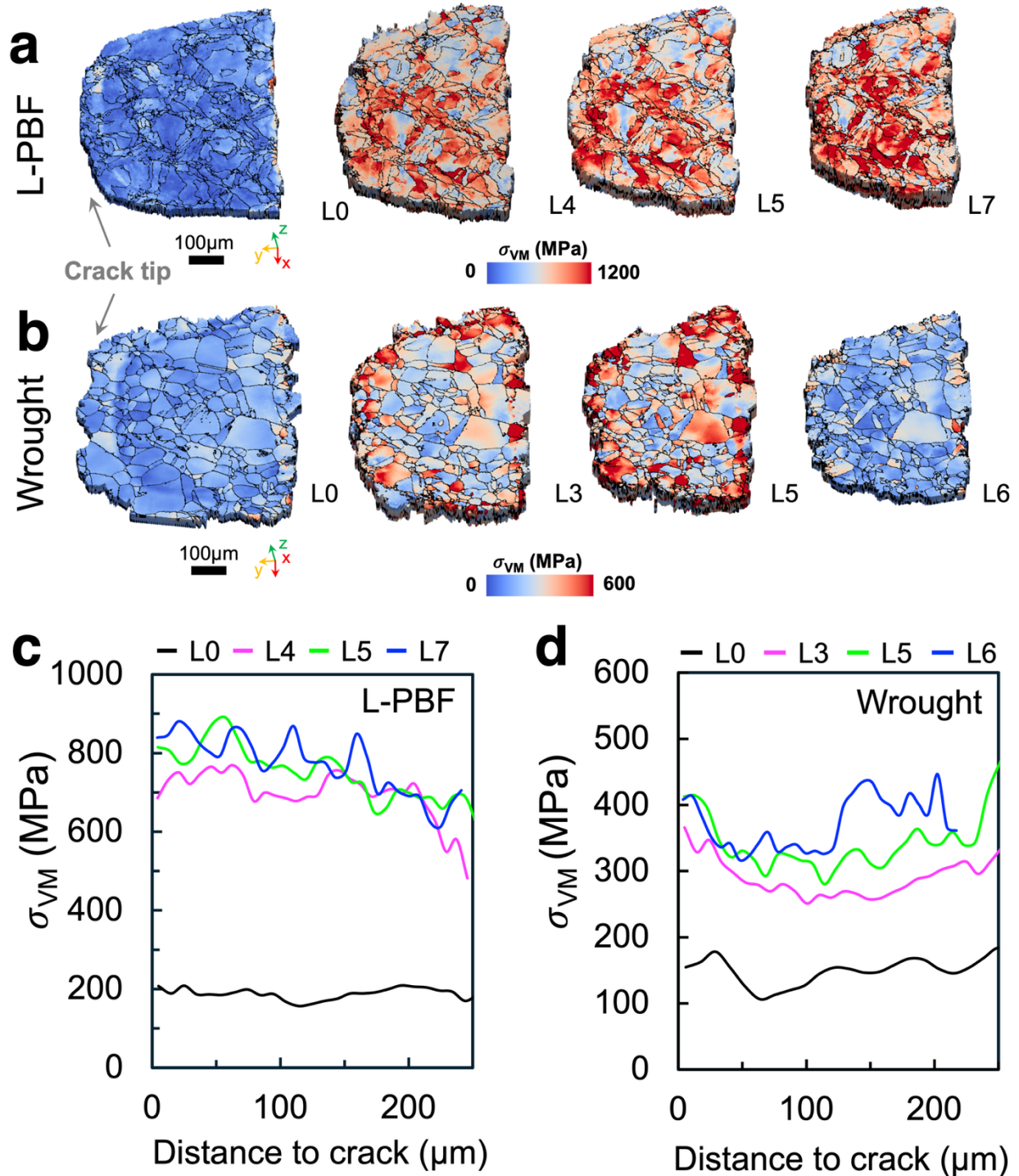


Fig. 6. Intragranular von Mises stress maps near the crack tip. (a) L-PBF specimen showing high stress retention (>800 MPa) and localized hotspots. (b) Wrought specimen showing effective stress relaxation and homogeneous distribution.

3.3.2 Stress triaxiality and Lode angle parameter

Beyond the scalar magnitude of internal stress, the local stress state was investigated to identify the crack-driving forces responsible for the observed transition from blunting to localized sharpening in the L-PBF sample. This was achieved by evaluating grain-averaged damage metrics, specifically stress triaxiality (η) and the Lode parameter (μ_σ). Stress triaxiality (η) is defined as the ratio of the mean stress (σ_m), or hydrostatic stress to the von Mises stress (σ_{VM}) expressed as:

$$\eta = \frac{\sigma_m}{\sigma_{VM}} \quad (7)$$

where the mean stress is derived from the first invariant of the stress tensor ($\sigma_m = I_1/3$). The Lode parameter (μ_σ) was further utilized to characterize the deviatoric stress state, defined using the principal stresses ($\sigma_1, \sigma_2, \sigma_3$):

$$\mu_\sigma = \left(\frac{2\sigma_2 - \sigma_1 - \sigma_3}{\sigma_1 - \sigma_3} \right) \quad (8)$$

These parameters together provide a comprehensive view of the multiaxial stress state governing the region surrounding the crack tip.

The spatial distribution and line profiles of stress triaxiality confirm the presence of high stress concentrations localized at the crack tip for both specimens. As expected, strong triaxiality is observed near the notch, with peak η values for both L-PBF and wrought samples reaching between ~ 1.0 and 1.2 . However, the spatial gradient of these fields differs significantly. The L-PBF specimen maintains a broad region of high triaxiality that remains positive (above 0.5) for nearly $150 \mu\text{m}$ (extending to $175 \mu\text{m}$ at the final load step, L7) from the crack tip before fluctuating (**Fig. 7a**). This behavior is consistent with the elevated von Mises stresses observed near the crack tip in Section 3.3.1. Furthermore, the L-PBF material exhibits a sharp transition from high triaxiality (approximately 1.0 – 1.5) to near-zero values immediately at the crack tip, indicating that the stress state localizes into a thin band.

In contrast, the wrought material displays a much steeper triaxiality gradient (**Fig. 7b**). After peaking at the notch, η drops sharply and transitions into a compressive state ($\eta \sim 0.8$) within approximately $100 \mu\text{m}$ of the crack tip. The spatial map at L6 clearly illustrates this transition from a concentrated tensile "hotspot" at the tip to a broad compressive zone in the far-field (starting at $\sim 85 \mu\text{m}$ from the tip). This rapid decay in triaxiality is consistent with the stress relaxation observed in the wrought sample, where localized plasticity effectively moderates the far-field stress state.

The Lode parameter further distinguishes the local mechanical environment of the two specimens. For the L-PBF specimen, μ_σ fluctuations remain predominantly negative near the crack tip, generally ranging between 0 and -0.25 (**Fig. 7c**), with an average value of -0.13 . The spatial map at L7 depicts this graphically, dominated by blue and cyan hues that indicate a uniform deviatoric state across the measured volume. The distributions for the L-PBF sample (particularly at L4, L5, and L7) hover around an average Lode angle of 0 , indicative of a pure shear state. Conversely, the wrought specimen displays a more complex response (**Fig. 7d**). The stress paths (L3, L5, L6) show greater fluctuation and remain further from the pure shear condition. Near the crack tip, the wrought material exhibits largely positive Lode angles (up to ~ 0.20), with an average μ_σ of 0.08 at L6. The spatial map for the wrought sample at L6 reflects this complexity, showing a varied mixture of red (positive) and blue (negative) regions throughout the grain structure. These visual maps confirm that the L-PBF microstructure is more anisotropic and sensitive to the Lode parameter, likely exacerbated by retained internal manufacturing defects (e.g., pores, oxides) that remain from the build process [46].

Collectively, these data imply that the L-PBF material is more susceptible to shear-controlled fracture mechanisms—which often result in lower ductility—whereas the wrought material handles a wider range of stress states more robustly [46]. The wrought material’s capacity for localized plastic flow leads to a more complex and relaxed redistribution of internal stresses. These differing internal stress states (e.g., σ_{VM} , η , and μ_σ) are intrinsically linked to microstructural differences, which are further analyzed via the evolution of dislocation substructures and GND distributions in Section 3.4.

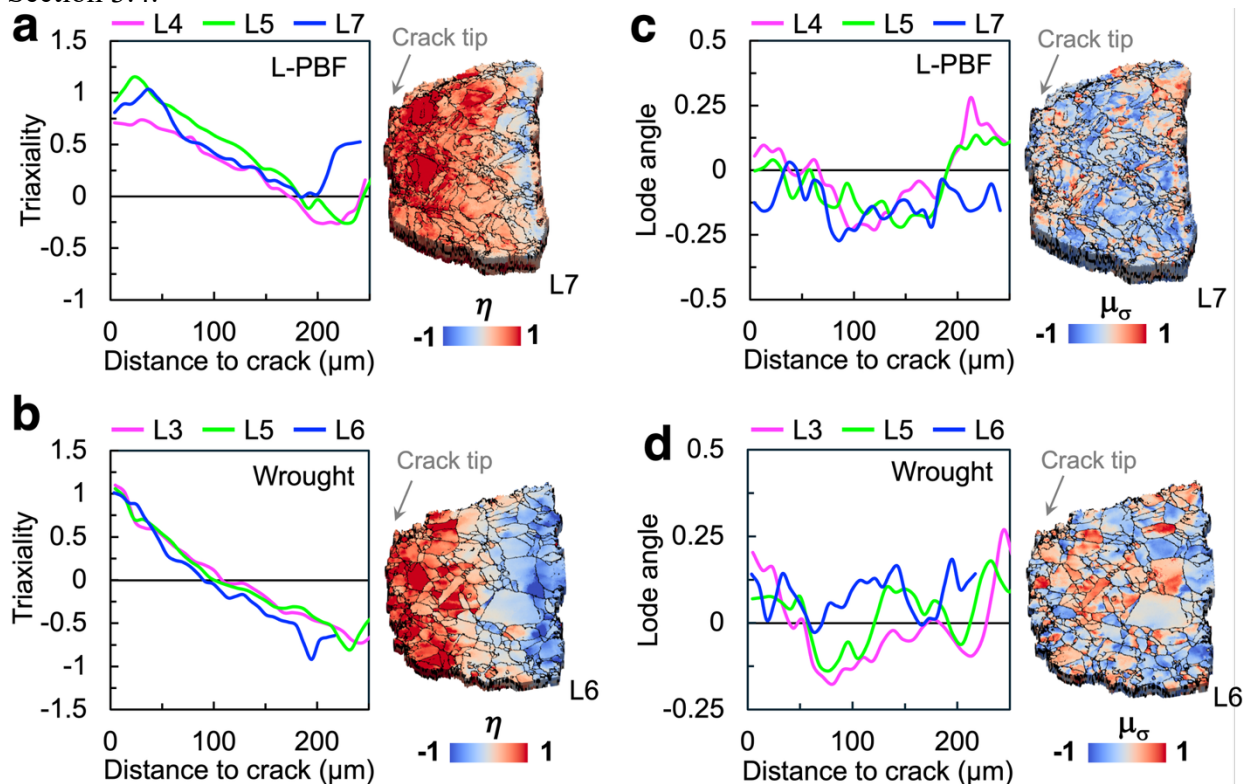


Fig. 7. Stress state analysis. (a-b) Spatial maps and line profiles of stress triaxiality (η). (c-d) Distributions of the Lode angle parameter (μ_σ) for both materials.

3.4 Dislocation density

To elucidate the micromechanical origins of the crack-tip stress states identified in Section 3.3, geometrically necessary dislocation density (ρ_{GND}) was quantified for both samples throughout loading. This analysis provides a direct measure of the local lattice curvature and plastic strain gradients required to maintain compatibility during deformation. GND densities were calculated via the Nye tensor method [47] using voxelized orientations extracted from the s3DXRD data and processed within the MTEX toolbox [47].

Fig. 8 presents the spatial evolution of ρ_{GND} throughout the loading sequence. A striking disparity is immediately evident in the initial (L0) state. The L-PBF material exhibits a high baseline dislocation density ($\sim 10^{15} \text{ m}^{-2}$) distributed throughout the microstructure (**Fig. 8a**), a remnant of the rapid thermal cycles and residual stresses inherent to the printing process [36]. In contrast, the wrought baseline shows a negligible initial GND population (**Fig. 8b**), characteristic of a fully annealed structure. The evolution of these distributions under load reveals fundamentally different plasticity mechanisms. In the wrought sample, ρ_{GND} evolves dynamically; a distinct concentration forms at the notch root by stage L3 and intensifies through L6, developing into a classic, highly

localized plastic zone. This localized accumulation accommodates the steep strain gradient at the crack tip, effectively blunting the geometrical stress concentration and facilitating the stress relaxation observed in the von Mises profiles [26]. Conversely, the L-PBF sample exhibits a remarkable lack of microstructural evolution. Despite increasing macroscopic load, the ρ_{GND} distribution remains spatially stagnant, showing no significant accumulation at the notch tip or reorganization into a defined plastic zone. Instead, dislocation density remains high and dispersed globally, with no correlation to the local stress field.

Quantitative line profiles extracted from the crack tip into the interior further clarify this behavior (Fig. 9). While the wrought material develops a steep GND gradient—peaking at the crack tip surface and decaying into the bulk—the L-PBF material maintains a uniform plateau across the first 150 μm of the process zone throughout the entire loading range (Fig. 9a). This absence of gradient formation suggests that the pre-existing substructure in L-PBF is already at or near dislocation saturation. The material is therefore unable to generate the necessary geometrically necessary dislocations to accommodate the crack-tip singularity. Consequently, instead of blunting, the crack tip retains high-magnitude internal stresses (as shown in Sections 3.3.1 and 3.3.2), driving the failure mechanism toward the shear localization instability described in the previous section.

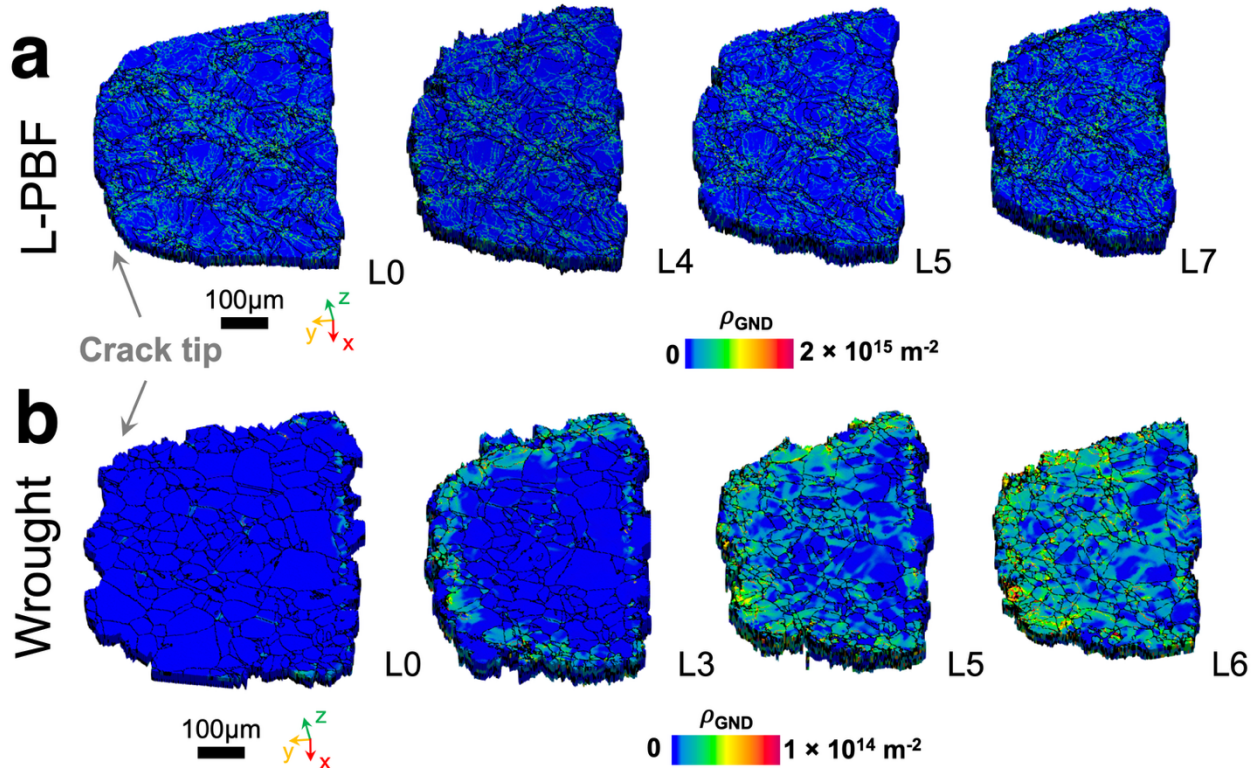


Fig. 8. Geometrically Necessary Dislocation (GND) density (ρ_{GND}) maps at the crack tip. (a) L-PBF specimen showing stagnant baseline density across load steps. (b) Wrought specimen showing evolution of a high-density plastic zone.

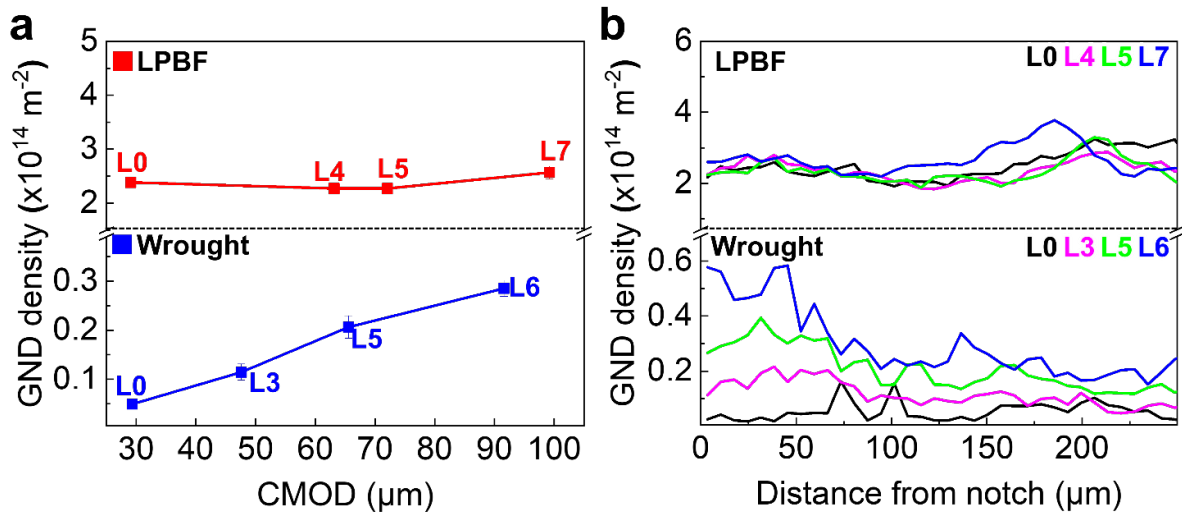


Fig. 9. GND density line profiles from the notch surface. (a) L-PBF profiles showing a uniform plateau. (b) Wrought profiles showing a steep decay from the notch tip whereas LPBF shows largely uniform spatial distributions of GND.

4. Discussion

The central objective of this study was to resolve the long-standing “toughness paradox” in L-PBF alloys, namely: *why materials that exhibit exceptional strength and uniform tensile ductility fail prematurely in the presence of a sharp crack?* By combining *in-situ* PCT with scanning s3DXRD, we directly interrogated subsurface crack-tip micromechanics in bulk material—conditions under which fracture toughness is governed. The resulting data allow us to critically re-evaluate prevailing hypotheses for reduced toughness in AM alloys and establish a unified, mechanistic explanation rooted in constrained crack-tip plasticity.

4.1 Role of AM process defects: necessary but not sufficient

A dominant narrative in the AM literature attributes low fracture toughness to processing-induced defects such as porosity and oxide inclusions [1,5,9]. While processing defects may play important roles in reducing bulk toughness in material made with non-optimized processing variables (e.g., >0.5% bulk porosity) or in influencing crack path selection [48], our results demonstrate microscale processing defects are not the primary origin of the dramatic toughness deficit observed in L-PBF 316L. This is based on quantitative PCT measurements, which revealed that both L-PBF and wrought specimens are effectively fully dense (>99.9%), with statistically similar pore size distributions and maximum defect sizes within the probed volume (**Fig. 1c-d**). These subtle differences cannot plausibly account for the ~40–70% reduction in conditional fracture toughness measured for the L-PBF material in the context of classical defect-centric fracture frameworks such as Rice-Tracey or Gurson-Tvergaard-Needleman models [10,12].

Instead, the interaction between the crack tip and defects differs fundamentally between the two microstructures. In the wrought alloy, cracks maintain a blunted morphology as they encounter pores, smoothly incorporating them without triggering new failure fronts (**Fig. 3**). Even when considering the morphological evolution of the pore prior to its interaction with the crack, the observed elongation suggests that the microstructure surrounding the crack tip is capable of accommodating deformation effectively. These behaviors indicate sufficient local plasticity to

accommodate the amplified stress concentration at the pore–crack junction; such behaviors are well known in wrought austenitic stainless steels to enable exceptional damage tolerance [49]. In contrast, the L-PBF alloy exhibits premature sharp crack initiation when approaching even isolated pores without noticeable shape evolution. Rather than serving as arrest sites, pores act as preferred coalescence targets, promoting rapid void capture and unstable crack advance. These observations indicate that porosity acts as an amplifier of an already unstable crack-tip state in L-PBF, not its root cause. Therefore, continued reductions in bulk defect density alone are therefore unlikely to yield substantial gains in fracture toughness unless the intrinsic crack-tip plasticity of the L-PBF microstructure is simultaneously improved. This may explain why recent approaches leveraging intrinsic toughening at the microstructural scale via multi-phase cellular structures in $\text{Al}_{0.5}\text{CrCoFeNi}$ have led to significantly improved fracture toughness [20], whereas extrinsic toughness modification solely via porosity control have shown more modest improvements [50,51].

We therefore propose that the fracture mechanism in L-PBF SS316L is controlled not by the gradual development of a damage process zone, but by the intrinsic inability of the material to harden further, leading to a sharp, unstable fracture path that bypasses the energy-dissipating process of widespread void formation observed in the wrought counterpart. Consequently, this would also suggest that timeframe between void nucleation and coalescence in L-PBF is negligible, largely bypassing the stable void growth regime predicted by Rice-Tracey mechanics and resulting in failure driven by immediate shear instability [10]. The exhaustion of work hardening capability triggers macroscopic strain localization rather than void coalescence, leading to the observed rapid fracture. Nanoscale void nucleation at oxides (below the $\sim 2\mu\text{m}$ resolution limit for a pixel size of $0.93\mu\text{m}$) cannot be ruled out; however, even if nanoscale voids nucleate, the stagnant GND density confirms that they cannot grow via conventional plasticity mechanisms [11]. Furthermore, similar reductions in toughness exist for SPD deformed materials, of which have relatively “clean” microstructures (e.g., largely absent of the large numbers of oxides in AM) [13,52,53]. Additional analyses on initiation, growth, and coalescence in L-PBF alloys with sub-micron resolution are warranted to further quantify the local role of nanoscale features (such as oxides, precipitates, and the cellular dislocation structure itself) on fracture mechanisms and overall toughness reduction.

4.2 Crack-tip plasticity exhaustion

The *in-situ* s3DXRD analysis reveals a fundamental difference in the micromechanical response of the L-PBF and wrought materials, specifically regarding their capacity to manage crack-tip singularities. While both materials exhibit comparable average von Mises stresses in the initial unloaded state, their evolution under load follows distinct pathways that dictate their fracture resistance (**Fig. 5**). The wrought alloy exhibits a classical ductile fracture response, governed by the progressive evolution of a crack-tip plastic zone. As load increases, the material accommodates the crack-tip strain gradient through significant dislocation multiplication, evidenced by the development of a steep GND density gradient at the notch root (**Fig. 8a**). This microstructural evolution facilitates effective stress relaxation: intragranular von Mises stresses generally plateau near the macroscopic flow stress (**Fig. 6b**), while stress triaxiality peaks sharply at the crack tip before decaying rapidly into the bulk. This behavior characterizes a material capable of continuous work hardening, which enables stable crack-tip blunting and a rising R-curve (resistance to crack extension) [54,55].

In contrast, the L-PBF sample shows the extreme internal stress buildup, where average σ_{VM} rapidly exceeds the macroscopic YS (as early as L4) and, locally, even the ultimate tensile strength

(Fig. 6a). These elevated stresses are not confined to the immediate crack tip but persist over a broad region ahead of the crack, accompanied by sustained high stress triaxiality (Fig. 7a). Crucially, this internal stress buildup is not accompanied by commensurate plastic relaxation as already high ρ_{GND} shows little additional accumulation during crack advance, and locally little correlation with distance to the crack tip stress singularity (Fig. 9b). This indicates premature work-hardening saturation or dislocation exhaustion mechanisms [56,57] where the microstructure lacks the capacity to store additional dislocations and thereby relax crack-tip constraints. This interpretation is supported by recent micromechanical studies by Li et al. [58] confirm that the YS of L-PBF SS316L is governed primarily by its high pre-existing dislocation density rather than cell size. Our work extends this understanding to the fracture regime, demonstrating that this same high initial dislocation density creates a 'saturation' ceiling, limiting the localized plasticity required for crack tip blunting.

This microstructural saturation has significant implications for continuum-level damage modeling. Recent works by Wilson-Heid and Beese [59] have successfully applied stress-state dependent damage models to predict failure in L-PBF stainless steels, utilizing the concept of ductility exhaustion. While such phenomenological models accurately predict *when* fracture occurs, they do not explicitly account for the microstructural origins of the reduced ductility limits. Our observation of dislocation saturation provides the physical basis for these parameters. According to the Considère criterion, plastic instability (necking or localized failure) initiates when the work-hardening rate drops below the flow stress ($d\sigma/d\varepsilon \leq \sigma$). In wrought material, the capacity for dislocation multiplication maintains a high hardening rate, delaying this instability. In L-PBF material, the pre-existing high dislocation density 'exhausts' this hardening capability almost immediately upon yielding. Consequently, the 'critical strain' used in ductility exhaustion models is reached rapidly—not necessarily due to void coalescence, but due to the inability of the matrix to distribute plastic strain via hardening. Thus, the 'work-hardening exhaustion' observed here acts as the physical precursor to the 'ductility exhaustion' modeled at the continuum scale.

This mechanistic link between dislocation saturation and reduced fracture resistance is not unique to AM; it parallels the behavior observed in materials processed via SPD or extensive cold work. For instance, Han et al. [60] demonstrated that iron processed by equal-channel angular pressing transitions from ductile to cleavage-like fracture due to the formation of high-energy dislocation structures that exhaust work-hardening capacity. Similarly, Chipperfield [13] showed in cold-worked 316 stainless steel that prior plastic deformation significantly reduces the crack opening displacement at initiation compared to the annealed state. In both cases—analogue to the L-PBF material studied here—the high pre-existing dislocation density precludes the generation of the steep GND gradients necessary for blunting, forcing the material to fail via localized shear bands or quasi-cleavage mechanisms despite exhibiting high ductility under uniaxial tension.

Overall, this analysis helps to resolve the apparent conflict between the high tensile ductility and low fracture toughness of L-PBF 316L: the introduction of a sharp notch and the resultant triaxial stress state expose a critical deficiency in hardening capacity that is less apparent under uniaxial loading. Furthermore, it is important to recognize that austenitic stainless steel represents a 'best-case scenario' for AM ductility due to its high strain hardening potential and high crystal symmetry [1,5]. The fact that work-hardening exhaustion compromises fracture resistance even in this inherently tough material suggests that the implications for less ductile alloy systems such as (Al-Si or Ti-6Al-4V) may be even more severe [5,61]. In these systems, where plasticity is already limited by restricted slip systems or brittle eutectic networks, the pre-exhausted state induced by

L-PBF processing acts as a critical vulnerability, rendering them catastrophically sensitive to notch-like defects.

4.3 Microstructural origins of orientation-dependent stress partitioning

The heterogeneous internal stress distributions observed in **Fig. 6** suggest that the local micromechanical response of the material is intimately linked to the local crystallographic orientation. While the macroscopic driving force dictates the general stress state, the localized von Mises “hotspots” observed particularly in the L-PBF material (**Fig. 6b**) appear to be a direct consequence of grain-level anisotropy [34]. To probe this orientation dependence, we interrogated a subset of internal grains situated within both the high-stress (>800 MPa) and low-stress (<400 MPa) regions of the crack-tip process zone. These grains were selected to span the IPF and distinct spatial locations relative to the crack tip, ensuring that the observed trends were not artifacts of proximity to the singularity but rather intrinsic to the crystal mechanics.

In the L-PBF material, grains exhibiting the highest retained von Mises stresses (g_1 and g_2) consistently associated with “hard” crystallographic orientations of $\langle 102 \rangle$ and $\langle 112 \rangle$ (**Fig. 10a**); these orientations have high directional strength-to-stiffness ratios [62], and effectively act as stress risers within the microstructure, unable to readily activate slip systems to accommodate the imposed strain via plastic deformation. Conversely, grains in the lower stress regime (g_3 and g_4) corresponded to orientations close to $\langle 110 \rangle$ which are favorable for slip and, based on strength to stiffness ratio, are thus expected to yield first. This distinct partitioning confirms that the load-bearing capacity of the L-PBF lattice is highly non-uniform. In the wrought counterpart, while a similar crystallographic dependence exists (e.g., “hard” grains g_i and g_{ii} and “soft” grains g_{iii} and g_{iv}), the magnitude of the stress gradient between hard and soft grains is significantly reduced (**Fig. 6b**). This suggests that the hierarchical microstructure of the L-PBF material further prevents the cooperative grain-to-grain load transfer that typically homogenizes stress fields in wrought alloys (**Fig. 6b**).

To further elucidate the mechanisms governing this stress retention, the intragranular misorientation spread is also plotted in **Fig. 10d** for the selected grain populations as a proxy for accumulated plastic strain and dislocation activity [63–65]. This analysis reveals a distinct inverse correlation between the magnitude of retained stress and the degree of internal misorientation, providing critical insight into the work-hardening state of the material. Specifically, the high-stress grains identified in the L-PBF material exhibit remarkably low internal misorientations (**Fig. 10d**). In a conventional ductile metal, high stress often accompanies high dislocation density; however, in this context, the low misorientation signifies a lack of recent plastic flow. We attribute this to dislocation hardening exhaustion: these grains retain high elastic stresses precisely because they cannot plastically deform further to relax the load. Conversely, the low-stress grains exhibit high degrees of misorientation, indicating they have undergone significant plasticity. These grains have successfully yielded, dissipating energy and shedding load via lattice rotation and sub-boundary formation [66].

Comparing the behaviors of wrought and L-PBF samples reveals a fundamental difference in how internal grains (those within the plastic zone but not directly at the crack tip), dissipate energy. In the wrought material, a broad population of grains exhibits high misorientations, confirming widespread plasticity that effectively shields the crack tip. In the L-PBF material, the prevalence of high-stress/low-misorientation grains indicates that a significant volume fraction of the material has reached a state of plastic saturation. This inability of internal grains to undergo plastic relaxation forces the crack tip to bear a higher effective driving force, directly triggering the transition to the unstable, sharp fracture modes discussed in Section 4.1.

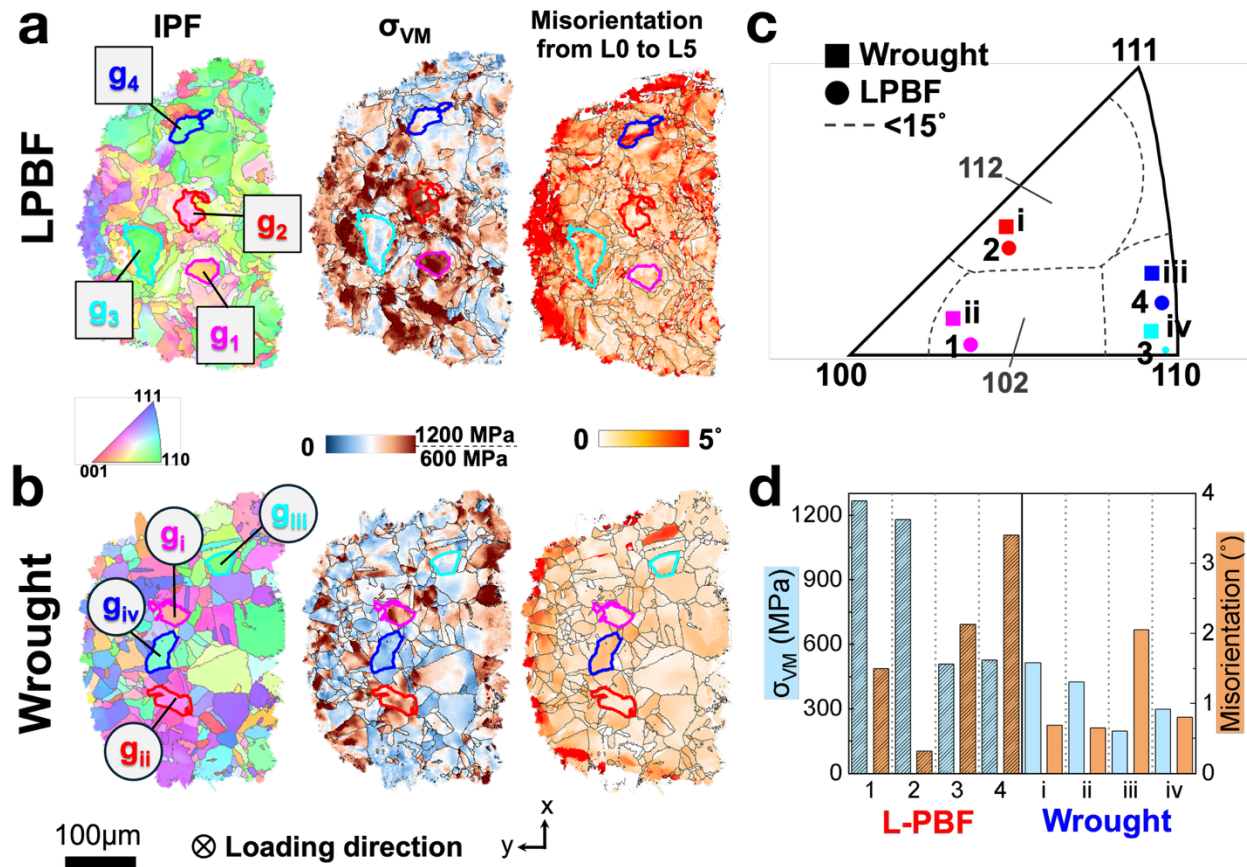


Fig. 10. Local analysis of stress partitioning in four representative grains spanning high- and low-stress regions and for (a) L-PBF, and (b) wrought samples. (c) IPF map showing grain orientations. (d) Relationship between stress and misorientation.

4.4 Secondary toughening mechanisms: limited role of DIMIT

Deformation-induced martensitic transformation (DIMIT) is a well-established secondary toughening mechanism in austenitic steels where phase transformation from FCC austenite (γ) to BCC martensite (α') dissipates energy and relaxes local stress concentrations at the crack tip [35,67]. The extent of this transformation was investigated to determine if differences in DIMIT activity contributed to the observed disparity in fracture resistance.

Analysis of the wrought specimen reveals a measurable, albeit minor, phase transformation (**Fig. 11**). The volume fraction of the BCC phase increased from an initial baseline of 0.1% at L0 to 0.55% at L6. While surface observations suggested potentially higher fractions (**Fig. 11b** and **c**), these likely encompass artifacts from sample preparation (i.e., wire EDM damage [68]) rather than bulk transformation. The internal diffraction data confirms that while DIMIT is active in the wrought material, its contribution to the overall energy dissipation remains secondary to the primary mechanism of dislocation-mediated plasticity.

In sharp contrast, the L-PBF alloy exhibits no statistically significant phase transformation during crack propagation. The BCC volume fraction remained effectively constant, moving from 0.2% at L0 to only 0.25% at L6. This suggests that DIMIT is effectively suppressed in the L-PBF material with this grain size under room temperature straining, which has been confirmed in other studies on L-PBF 316L [69]. We attribute this suppression to the mechanical stabilization of the

austenite phase, where the high initial dislocation density characteristic of the as-built L-PBF microstructure increases the critical stress required for martensitic nucleation. Furthermore, the limited extent of plastic deformation in the L-PBF sample (discussed in Section 4.2) restricts the mechanical work available to drive the transformation. Consequently, the L-PBF material is deprived of this secondary toughening mechanism, further compounding the ductility deficit caused by work-hardening exhaustion.

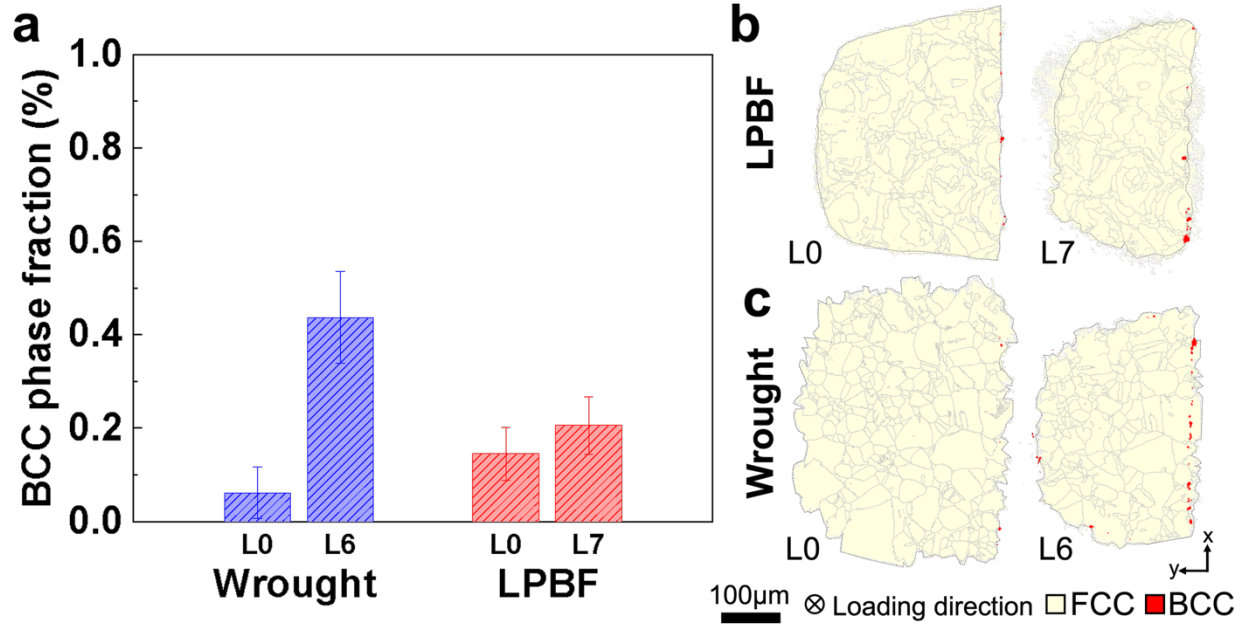


Fig. 11. Quantitative tracking of the BCC (martensite) volume fraction for L-PBF and wrought samples at initial and final s3DXRD measurements.

5. Conclusion

In this study, the fracture behavior of L-PBF 316L stainless steel was investigated using *in-situ* phase contrast tomography (PCT) and scanning 3D X-ray diffraction (s3DXRD) to elucidate the micromechanical origins of its reduced toughness. Overall, the following conclusions can be drawn:

- **The Toughness Paradox:** Despite exhibiting excellent strength and ductility under uniaxial tensile loading, the L-PBF material displays significantly reduced fracture toughness (measured via CTOD and conditional K_q) compared to its wrought counterpart, although both possess nearly identical grain sizes and initial defect densities. While the wrought material exhibits a rising R-curve behavior with extensive plasticity, the L-PBF material fails prematurely, highlighting a critical disconnect between uniaxial ductility and damage tolerance in complex AM microstructures.
- **Suppression of Crack-Tip Blunting:** *In-situ* PCT revealed that the toughness deficit originates geometrically from an inability to blunt the crack tip. The wrought material accommodates crack-tip singularities through significant blunting, reducing local stress concentrations. In contrast, the L-PBF material maintains a sharp crack-tip profile throughout loading. This sharp-crack propagation persists regardless of whether the crack interacts with process-induced

voids or fully dense material, indicating that the behavior is intrinsic to the microstructure rather than driven solely by extrinsic defects.

- **Failure of Stress Relaxation:** *In-situ* s3DXRD mapping of the specimen interior demonstrated that the sharp crack morphology in L-PBF stems from a fundamental inability to relax crack-tip stresses. While the wrought material effectively limits lattice stress buildup through plastic dissipation, the L-PBF material develops extreme internal stresses that rapidly exceed the macroscopic ultimate tensile strength over a broad region ahead of the crack tip.
- **Work-Hardening Exhaustion:** The lack of stress relaxation is driven by the exhaustion of work-hardening capacity. Analysis of GND densities shows that the pre-existing dislocation network in the L-PBF material ($\sim 10^{15} \text{ m}^{-2}$) is stagnant; it does not evolve or grow into a defined plastic zone near the crack tip. Conversely, the wrought material develops a steep GND gradient, confirming the generation of new dislocations to accommodate local strain.
- **Grain-Scale Stress Partitioning:** Local analysis reveals that stress accumulation in the L-PBF microstructure is strongly dependent on grain orientation. A clear inverse correlation was observed where grains exhibiting high internal stresses possess low internal misorientations. This provides definitive evidence that highly stressed grains in the L-PBF lattice are elastically loaded to failure because they are unable to undergo the necessary plastic rotation and deformation required to blunt the crack.

These findings indicate that the "toughness paradox" in L-PBF is not primarily a defect-controlled phenomenon but an intrinsic consequence of the hierarchical, high-dislocation microstructure. The pre-saturated dislocation network prevents the localized plasticity required for blunting, leading to brittle-like fracture in a nominally ductile alloy under high stress triaxialities. Since SS316L is among the most ductile AM alloys available, this exhaustion mechanism serves as a conservative warning for less forgiving systems (e.g., Ti-6Al-4V, AlSi10Mg). Future alloy design for damage-tolerant AM components must therefore prioritize not just high yield strength, but the restoration of work-hardening capacity through heat treatment or alloy modification to recover the material's ability to manage crack-tip singularities.

Acknowledgements

We are grateful to the ESRF for the provision of beamtime on ID11 under proposal numbers MA-6524. This work was partially supported by NSF DMR- 2237433. The authors acknowledge the financial support of the University of Michigan College of Engineering and NSF grant #DMR-0320740, and technical support from the Michigan Center for Materials Characterization.

References

- [1] T.H. Becker, P. Kumar, U. Ramamurty, Fracture and fatigue in additively manufactured metals, *Acta Mater.* 219 (2021). <https://doi.org/10.1016/j.actamat.2021.117240>.
- [2] J.J. Lewandowski, M. Seifi, *Metal Additive Manufacturing: A Review of Mechanical Properties*, *Annu. Rev. Mater. Res.* 46 (2016) 151–186. <https://doi.org/10.1146/annurev-matsci-070115-032024>.

- [3] W. Chen, T. Voisin, Y. Zhang, J.B. Florien, C.M. Spadaccini, D.L. McDowell, T. Zhu, Y.M. Wang, Microscale residual stresses in additively manufactured stainless steel, *Nat. Commun.* 10 (2019). <https://doi.org/10.1038/s41467-019-12265-8>.
- [4] Y.M. Wang, T. Voisin, J.T. McKeown, J. Ye, N.P. Calta, Z. Li, Z. Zeng, Y. Zhang, W. Chen, T.T. Roehling, R.T. Ott, M.K. Santala, P.J. Depond, M.J. Matthews, A. V. Hamza, T. Zhu, Additively manufactured hierarchical stainless steels with high strength and ductility, *Nat. Mater.* 17 (2018) 63–70. <https://doi.org/10.1038/NMAT5021>.
- [5] M.J. Paul, J.J. Kruzic, U. Ramamurty, B. Gludovatz, The importance of fracture toughness evaluation for additively manufactured metals, *Acta Mater.* 276 (2024). <https://doi.org/10.1016/j.actamat.2024.120061>.
- [6] W.J. Mills, Fracture toughness of type 304 and 316 stainless steels and their welds, 1997.
- [7] B.D. Snartland, C. Thaulow, Fracture toughness testing at the micro-scale – The effect of the unloading compliance method, *Eng. Fract. Mech.* 235 (2020). <https://doi.org/10.1016/j.engfracmech.2020.107135>.
- [8] J.F. Knott, Micro-mechanisms of fracture and the fracture toughness of engineering alloys, 1977.
- [9] S.L.B. Kramer, A. Jones, A. Mostafa, B. Ravaji, T. Tancogne-Dejean, C.C. Roth, M.G. Bandpay, K. Pack, J.T. Foster, M. Behzadinasab, J.C. Sobotka, J.M. McFarland, J. Stein, A.D. Spear, P. Newell, M.W. Czabaj, B. Williams, H. Simha, M. Gesing, L.N. Gilkey, C.A. Jones, R. Dingreville, S.E. Sanborn, J.L. Bignell, A.R. Cerrone, V. Keim, A. Nonn, S. Cooreman, P. Thibaux, N. Ames, D.O. Connor, M. Parno, B. Davis, J. Tucker, B. Coudrillier, K.N. Karlson, J.T. Ostien, J.W. Foulk, C.I. Hammett, S. Grange, J.M. Emery, J.A. Brown, J.E. Bishop, K.L. Johnson, K.R. Ford, S. Brinckmann, M.K. Neilsen, J. Jackiewicz, K. Ravi-Chandar, T. Ivanoff, B.C. Salzbrener, B.L. Boyce, The third Sandia fracture challenge: predictions of ductile fracture in additively manufactured metal, *Int. J. Fract.* 218 (2019) 5–61. <https://doi.org/10.1007/s10704-019-00361-1>.
- [10] J.R. Rice, D.A. Tracey, On the ductile enlargement of voids in triaxial stress fields, Pergamon Press, 1969.
- [11] P.J. Noell, R.B. Sills, A.A. Benzerga, B.L. Boyce, Void nucleation during ductile rupture of metals: A review, *Prog. Mater. Sci.* 135 (2023). <https://doi.org/10.1016/j.pmatsci.2023.101085>.
- [12] V. Tvergaard, A. Needleman, Analysis of the cup-cone fracture in a round tensile bar, 1984.
- [13] C.G. Chipperfield, Detection and toughness characterisation of ductile crack initiation in 316 stainless steels, *Int. J. Fract.* 12 (1976).
- [14] M. Kamaya, Elastic-plastic failure assessment of cold worked stainless steel pipes, *International Journal of Pressure Vessels and Piping* 131 (2015) 45–51. <https://doi.org/10.1016/j.ijpvp.2015.04.008>.
- [15] N. Wang, C. Wang, X. Liu, Y. Chen, G. Wu, L. Zhu, J. Luo, Influence of dislocation density on the fracture behavior of pipeline steel after plastic deformation damage, *Eng. Fail. Anal.* 177 (2025). <https://doi.org/10.1016/j.engfailanal.2025.109663>.
- [16] M. Danylenko, Y. Podrezov, S. Firstov, Effect of dislocation structure on fracture toughness of strained BCC-metals, *Theoretical and Applied Fracture Mechanics* 32 (1999) 914. www.elsevier.com/locate/tafmec.
- [17] P.J. Noell, J.D. Carroll, B.L. Boyce, The mechanisms of ductile rupture, *Acta Mater.* 161 (2018) 83–98. <https://doi.org/10.1016/j.actamat.2018.09.006>.

- [18] P.J. Noell, J.E.C. Sabisch, D.L. Medlin, J.D. Carroll, B.L. Boyce, Ductile failure—from the nanoscale origins of void nucleation to the mechanisms of ductile rupture, n.d. https://www.youtube.com/watch?v=xtxd27jIZ_g.
- [19] P. Kumar, R. Jayaraj, J. Suryawanshi, U.R. Satwik, J. McKinnell, U. Ramamurty, Fatigue strength of additively manufactured 316L austenitic stainless steel, *Acta Mater.* 199 (2020) 225–239. <https://doi.org/10.1016/j.actamat.2020.08.033>.
- [20] P. Kumar, S. Huang, D.H. Cook, K. Chen, U. Ramamurty, X. Tan, R.O. Ritchie, A strong fracture-resistant high-entropy alloy with nano-bridged honeycomb microstructure intrinsically toughened by 3D-printing, *Nat. Commun.* 15 (2024). <https://doi.org/10.1038/s41467-024-45178-2>.
- [21] G. Hahn, A. Rosenfield, Sources of Fracture Toughness: The Relation Between K_{Ic} and the Ordinary Tensile Properties of Metals, in: *Applications Related Phenomena in Titanium Alloys*, ASTM International 100 Barr Harbor Drive, PO Box C700, West Conshohocken, PA 19428-2959, 1968: pp. 5–32. <https://doi.org/10.1520/STP33617S>.
- [22] X. Li, Y. Wei, L. Lu, K. Lu, H. Gao, Dislocation nucleation governed softening and maximum strength in nano-twinned metals, *Nature* 464 (2010) 877–880. <https://doi.org/10.1038/nature08929>.
- [23] Y. Zhao, Y. Su, Y. Ding, X. Liu, J. Zhang, Y. Yan, B. Chen, Pixel-removing digital image correlation – a universal method for speckle pattern image degradation and cracking, *Eng. Fract. Mech.* 328 (2025). <https://doi.org/10.1016/j.engfracmech.2025.111569>.
- [24] E. Salvati, S. O’Connor, T. Sui, D. Nowell, A.M. Korsunsky, A study of overload effect on fatigue crack propagation using EBSD, FIB–DIC and FEM methods, *Eng. Fract. Mech.* 167 (2016) 210–223. <https://doi.org/10.1016/j.engfracmech.2016.04.034>.
- [25] P.J. Withers, Fracture mechanics by three-dimensional crack-tip synchrotron X-ray microscopy, *Philosophical Transactions of the Royal Society A: Mathematical, Physical and Engineering Sciences* 373 (2015). <https://doi.org/10.1098/rsta.2013.0157>.
- [26] Y. Zhang, J. Ball, A. Henningsson, J. Wright, L. Lopez, D. Jobes, H. Proudhon, J. V. Gordon, Unveiling 3D sub-grain residual stresses in as-built additively manufactured steel using scanning 3DXRD, *Mater. Res. Lett.* 13 (2025) 700–708. <https://doi.org/10.1080/21663831.2025.2502502>.
- [27] N. Gueninchault, H. Proudhon, W. Ludwig, Nanox: A miniature mechanical stress rig designed for near-field X-ray diffraction imaging techniques, *J. Synchrotron Radiat.* 23 (2016) 1474–1483. <https://doi.org/10.1107/S1600577516013850>.
- [28] G. Dehm, B.N. Jaya, R. Raghavan, C. Kirchlechner, Overview on micro- and nanomechanical testing: New insights in interface plasticity and fracture at small length scales, *Acta Mater.* 142 (2018) 248–282. <https://doi.org/10.1016/j.actamat.2017.06.019>.
- [29] J. Gordon, D. Rubio-Ejchel, D. Jobes, Y. Zhang, J. Ball, H. Proudhon, K. Ryou, C. Romain, Scanning-3DXRD measurement of crack tip orientation-strain states to elucidate ductile fracture mechanisms in 3D printed steels, 2026. <https://doi.org/10.1515/ESRF-DC-2354238808>.
- [30] H. Payno, P. Paleo, C. Nemoz, P. Cloetens, M. Di Michiel, A. Rack, P. Tafforeau, V.A. Solé, N.R. Viganò, Overcoming the data processing challenges of unifying tomography techniques at ESRF, in: *J. Phys. Conf. Ser.*, Institute of Physics, 2022. <https://doi.org/10.1088/1742-6596/2380/1/012106>.

- [31] Y. Hayashi, Y. Hirose, Y. Seno, Polycrystal orientation mapping using scanning three-dimensional X-ray diffraction microscopy, *J. Appl. Crystallogr.* 48 (2015) 1094–1101. <https://doi.org/10.1107/S1600576715009899>.
- [32] J. Wright, FABLE-3DXRD/ImageD11, (2020). <https://github.com/FABLE-3DXRD/ImageD11>.
- [33] J. Hektor, S.A. Hall, N.A. Henningsson, J. Engqvist, M. Ristinmaa, F. Lenrick, J.P. Wright, Scanning 3DXRD measurement of grain growth, stress, and formation of Cu 6 Sn 5 around a tin whisker during heat treatment, *Materials* 12 (2019). <https://doi.org/10.3390/ma12030446>.
- [34] A. Henningsson, M. Kutsal, J.P. Wright, W. Ludwig, H.O. Sørensen, S.A. Hall, G. Winther, H.F. Poulsen, Microstructure and stress mapping in 3D at industrially relevant degrees of plastic deformation, *Sci. Rep.* 14 (2024). <https://doi.org/10.1038/s41598-024-71006-0>.
- [35] J.A.D. Ball, C. Davis, C. Slater, H. Vashishtha, M. Said, L. Hébrard, F. Steinhilber, J.P. Wright, T. Connolley, S. Michalik, D.M. Collins, Grain-level effects on in-situ deformation-induced phase transformations in a complex-phase steel using 3DXRD and EBSD, *Acta Mater.* 265 (2024). <https://doi.org/10.1016/j.actamat.2023.119608>.
- [36] A. Mostafaei, C. Zhao, Y. He, S. Reza Ghiaasiaan, B. Shi, S. Shao, N. Shamsaei, Z. Wu, N. Kouraytem, T. Sun, J. Pauza, J. V. Gordon, B. Webler, N.D. Parab, M. Asherloo, Q. Guo, L. Chen, A.D. Rollett, Defects and anomalies in powder bed fusion metal additive manufacturing, *Curr. Opin. Solid State Mater. Sci.* 26 (2022). <https://doi.org/10.1016/j.cossms.2021.100974>.
- [37] A.Y. Al-Maharma, S.P. Patil, B. Markert, Effects of porosity on the mechanical properties of additively manufactured components: a critical review, *Mater. Res. Express* 7 (2020). <https://doi.org/10.1088/2053-1591/abcc5d>.
- [38] H. Toda, E. Maire, S. Yamauchi, H. Tsuruta, T. Hiramatsu, M. Kobayashi, In situ observation of ductile fracture using X-ray tomography technique, *Acta Mater.* 59 (2011) 1995–2008. <https://doi.org/10.1016/j.actamat.2010.11.065>.
- [39] M.A. Verstraete, R.M. Denys, K. Van Minnebruggen, S. Hertelé, W. De Waele, Determination of CTOD resistance curves in side-grooved Single-Edge Notched Tensile specimens using full field deformation measurements, *Eng. Fract. Mech.* 110 (2013) 12–22. <https://doi.org/10.1016/j.engfracmech.2013.07.015>.
- [40] J. Suryawanshi, K.G. Prashanth, U. Ramamurty, Mechanical behavior of selective laser melted 316L stainless steel, *Materials Science and Engineering: A* 696 (2017) 113–121. <https://doi.org/10.1016/j.msea.2017.04.058>.
- [41] Y. Hayashi, D. Setoyama, Y. Hirose, T. Yoshida, H. Kimura, Intragranular three-dimensional stress tensor fields in plastically deformed polycrystals, *Science* (1979). 366 (2019) 1492–1496. <https://www.science.org>.
- [42] N. Wawrzyniak, P.R. Provencher, M. Brochu, M. Brochu, Tensile properties of SS316L produced by LPBF: Influence of specimen dimensions and surface condition, *Mater. Charact.* 203 (2023). <https://doi.org/10.1016/j.matchar.2023.113117>.
- [43] Z. Li, T. Voisin, J.T. McKeown, J. Ye, T. Braun, C. Kamath, W.E. King, Y.M. Wang, Tensile properties, strain rate sensitivity, and activation volume of additively manufactured 316L stainless steels, *Int. J. Plast.* 120 (2019) 395–410. <https://doi.org/10.1016/j.ijplas.2019.05.009>.

- [44] T.S. Byun, B.E. Garrison, M.R. McAlister, X. Chen, M.N. Gussev, T.G. Lach, A. Le Coq, K. Linton, C.B. Joslin, J.K. Carver, F.A. List, R.R. Dehoff, K.A. Terrani, Mechanical behavior of additively manufactured and wrought 316L stainless steels before and after neutron irradiation, *Journal of Nuclear Materials* 548 (2021). <https://doi.org/10.1016/j.jnucmat.2021.152849>.
- [45] N.Y. Juul, J. Oddershede, A. Beaudoin, K. Chatterjee, M.K.A. Koker, D. Dale, P. Shade, G. Winther, Measured resolved shear stresses and Bishop-Hill stress states in individual grains of austenitic stainless steel, *Acta Mater.* 141 (2017) 388–404. <https://doi.org/10.1016/j.actamat.2017.09.021>.
- [46] A.A. Benzerga, J.B. Leblond, Ductile Fracture by Void Growth to Coalescence, 2010. [https://doi.org/10.1016/S0065-2156\(10\)44003-X](https://doi.org/10.1016/S0065-2156(10)44003-X).
- [47] F. Bachmann, R. Hielscher, H. Schaeben, Grain detection from 2d and 3d EBSD data- Specification of the MTEX algorithm, *Ultramicroscopy* 111 (2011) 1720–1733. <https://doi.org/10.1016/j.ultramic.2011.08.002>.
- [48] R. Muro-Barrios, Y. Cui, J. Lambros, H.B. Chew, Dual-scale porosity effects on crack growth in additively manufactured metals: 3D ductile fracture models, *J. Mech. Phys. Solids* 159 (2022). <https://doi.org/10.1016/j.jmps.2021.104727>.
- [49] A. Hilhorst, P.J. Jacques, T. Pardoen, Towards the best strength, ductility, and toughness combination: High entropy alloys are excellent, stainless steels are exceptional, *Acta Mater.* 260 (2023). <https://doi.org/10.1016/j.actamat.2023.119280>.
- [50] M. Jamshidian, P. Promoppatum, U. Ramamurty, M.H. Jhon, Modulating fracture toughness through processing-mediated mesostructure in additively manufactured Al-12Si alloy, *Mater. Des.* 215 (2022). <https://doi.org/10.1016/j.matdes.2022.110440>.
- [51] K.M. Conway, C. Kunka, B.C. White, G.J. Pataky, B.L. Boyce, Increasing fracture toughness via architected porosity, *Mater. Des.* 205 (2021). <https://doi.org/10.1016/j.matdes.2021.109696>.
- [52] X. Yang, F. Tang, X. Hao, Z. Li, Oxide Evolution During the Solidification of 316L Stainless Steel from Additive Manufacturing Powders with Different Oxygen Contents, *Metallurgical and Materials Transactions B: Process Metallurgy and Materials Processing Science* 52 (2021) 2253–2262. <https://doi.org/10.1007/s11663-021-02191-w>.
- [53] A. Hohenwarter, R. Pippan, Fracture and fracture toughness of nanopolycrystalline metals produced by severe plastic deformation, *Philosophical Transactions of the Royal Society A: Mathematical, Physical and Engineering Sciences* 373 (2015). <https://doi.org/10.1098/rsta.2014.0366>.
- [54] M.A. Verstraete, W. De Waele, K. Van Minnebruggen, S. Hertelé, Single-specimen evaluation of tearing resistance in SENT testing, *Eng. Fract. Mech.* 148 (2015) 324–336. <https://doi.org/10.1016/j.engfracmech.2015.07.067>.
- [55] S. Cravero, C. Ruggieri, Estimation procedure of J-resistance curves for SE(T) fracture specimens using unloading compliance, *Eng. Fract. Mech.* 74 (2007) 2735–2757. <https://doi.org/10.1016/j.engfracmech.2007.01.012>.
- [56] A. Salandari-Rabori, V. Fallah, Heterogeneity of deformation, shear band formation and work hardening behavior of as-printed AlSi10Mg via laser powder bed fusion, *Materials Science and Engineering: A* 866 (2023). <https://doi.org/10.1016/j.msea.2023.144698>.
- [57] Z. Li, Z. Li, Z. Tan, D.B. Xiong, Q. Guo, Stress relaxation and the cellular structure-dependence of plastic deformation in additively manufactured AlSi10Mg alloys, *Int. J. Plast.* 127 (2020). <https://doi.org/10.1016/j.ijplas.2019.12.003>.

- [58] Z. Li, B. He, Q. Guo, Strengthening and hardening mechanisms of additively manufactured stainless steels: The role of cell sizes, *Scr. Mater.* 177 (2020) 17–21. <https://doi.org/10.1016/j.scriptamat.2019.10.005>.
- [59] A.E. Wilson-Heid, A.M. Beese, Combined effects of porosity and stress state on the failure behavior of laser powder bed fusion stainless steel 316L, *Addit. Manuf.* 39 (2021). <https://doi.org/10.1016/j.addma.2021.101862>.
- [60] B.Q. Han, E.J. Lavernia, F.A. Mohamed, Dislocation Structure and Deformation in Iron Processed by Equal-Channel-Angular Pressing, n.d.
- [61] E.T. Furton, A.M. Beese, Ductile fracture model describing the impact of internal pores: Model development and validation for additively manufactured Ti-6Al-4V, *Addit. Manuf.* 102 (2025). <https://doi.org/10.1016/j.addma.2025.104722>.
- [62] S.L. Wong, P.R. Dawson, Influence of directional strength-to-stiffness on the elastic-plastic transition of fcc polycrystals under uniaxial tensile loading, *Acta Mater.* 58 (2010) 1658–1678. <https://doi.org/10.1016/j.actamat.2009.11.009>.
- [63] A.T. Polonsky, W.C. Lenthe, M.P. Echlin, V. Livescu, G.T. Gray, T.M. Pollock, Solidification-driven orientation gradients in additively manufactured stainless steel, *Acta Mater.* 183 (2020) 249–260. <https://doi.org/10.1016/j.actamat.2019.10.047>.
- [64] S. Subedi, R. Pokharel, A.D. Rollett, Orientation gradients in relation to grain boundaries at varying strain level and spatial resolution, *Materials Science and Engineering: A* 638 (2015) 348–356. <https://doi.org/10.1016/j.msea.2015.04.051>.
- [65] M. Calcagnotto, D. Ponge, E. Demir, D. Raabe, Orientation gradients and geometrically necessary dislocations in ultrafine grained dual-phase steels studied by 2D and 3D EBSD, *Materials Science and Engineering A* 527 (2010) 2738–2746. <https://doi.org/10.1016/j.msea.2010.01.004>.
- [66] D. Raabe, Z. Zhao, S.-J. Park, F. Roters, Theory of orientation gradients in plastically strained crystals, 2002. www.elsevier.com/locate/actamat.
- [67] S.M. Hasan, A. Ghosh, D. Chakrabarti, S.B. Singh, Deformation-induced martensite transformation and variant selection in AISI 316L austenitic stainless steel during uniaxial tensile deformation, *Materials Science and Engineering: A* 872 (2023). <https://doi.org/10.1016/j.msea.2023.144930>.
- [68] R. Prathipati, S.P. Dora, R. Chanamala, Wear behavior of wire electric discharge machined surface of 316L stainless steel, *SN Appl. Sci.* 2 (2020). <https://doi.org/10.1007/s42452-020-2244-z>.
- [69] Y. Hong, C. Zhou, Y. Zheng, L. Zhang, J. Zheng, X. Chen, B. An, Formation of strain-induced martensite in selective laser melting austenitic stainless steel, *Materials Science and Engineering: A* 740–741 (2019) 420–426. <https://doi.org/10.1016/j.msea.2018.10.121>.